

*ARMY RESEARCH LABORATORY*



---

**Flight Performance of a Man Portable Guided Projectile  
Concept**

**by Frank Fresconi, James DeSpirito, and Ilmars Celmins**

---

**ARL-TR-6840**

**February 2014**

## **NOTICES**

### **Disclaimers**

The findings in this report are not to be construed as an official Department of the Army position unless so designated by other authorized documents.

Citation of manufacturer's or trade names does not constitute an official endorsement or approval of the use thereof.

Destroy this report when it is no longer needed. Do not return it to the originator.

# **Army Research Laboratory**

Aberdeen Proving Ground, MD 21005-5066

---

---

**ARL-TR-6840**

**February 2014**

---

---

## **Flight Performance of a Man Portable Guided Projectile Concept**

**Frank Fresconi, James DeSpirito, and Ilmars Celmins  
Weapons and Materials Research Directorate, ARL**

<b>REPORT DOCUMENTATION PAGE</b>			<b>Form Approved OMB No. 0704-0188</b>		
Public reporting burden for this collection of information is estimated to average 1 hour per response, including the time for reviewing instructions, searching existing data sources, gathering and maintaining the data needed, and completing and reviewing the collection information. Send comments regarding this burden estimate or any other aspect of this collection of information, including suggestions for reducing the burden, to Department of Defense, Washington Headquarters Services, Directorate for Information Operations and Reports (0704-0188), 1215 Jefferson Davis Highway, Suite 1204, Arlington, VA 22202-4302. Respondents should be aware that notwithstanding any other provision of law, no person shall be subject to any penalty for failing to comply with a collection of information if it does not display a currently valid OMB control number. <b>PLEASE DO NOT RETURN YOUR FORM TO THE ABOVE ADDRESS.</b>					
<b>1. REPORT DATE (DD-MM-YYYY)</b> February 2014		<b>2. REPORT TYPE</b> Final		<b>3. DATES COVERED (From - To)</b> October 2012–September 2013	
<b>4. TITLE AND SUBTITLE</b> Flight Performance of a Man Portable Guided Projectile Concept			<b>5a. CONTRACT NUMBER</b>		
			<b>5b. GRANT NUMBER</b>		
			<b>5c. PROGRAM ELEMENT NUMBER</b>		
<b>6. AUTHOR(S)</b> Frank Fresconi, James DeSpirito, and Ilmars Celmins			<b>5d. PROJECT NUMBER</b> AH43		
			<b>5e. TASK NUMBER</b>		
			<b>5f. WORK UNIT NUMBER</b>		
<b>7. PERFORMING ORGANIZATION NAME(S) AND ADDRESS(ES)</b> U.S. Army Research Laboratory ATTN: RDRL-WML-E Aberdeen Proving Ground, MD 21005-5066			<b>8. PERFORMING ORGANIZATION REPORT NUMBER</b> ARL-TR-6840		
<b>9. SPONSORING/MONITORING AGENCY NAME(S) AND ADDRESS(ES)</b>			<b>10. SPONSOR/MONITOR'S ACRONYM(S)</b>		
			<b>11. SPONSOR/MONITOR'S REPORT NUMBER(S)</b>		
<b>12. DISTRIBUTION/AVAILABILITY STATEMENT</b> Approved for public release; distribution is unlimited.					
<b>13. SUPPLEMENTARY NOTES</b>					
<b>14. ABSTRACT</b> Future enhanced lethal effects at the squad level likely include precision guided technologies. The focus of this study is maneuvering projectiles launched from man portable weapon systems. A novel guided projectile concept is proposed for achieving control authority requirements in the challenging environment of low-dynamic pressure, small size, high-launch loads, spin-stabilization, and low cost. This new maneuver concept is based on a rotating wing actuator. Experimental and advanced computational aerodynamics techniques were applied. Aerodynamic models and projectile flight mechanics were derived to enable flight simulation. Assessment of ballistic delivery accuracy, based on physics-based models of the delivery process, was undertaken to quantify control authority requirements. Maneuvering flight simulations demonstrated that this concept affords enough course correction to compensate for ballistic delivery errors.					
<b>15. SUBJECT TERMS</b> projectile, spin-stabilized, maneuver, aeromechanics, man portable precision, guidance					
<b>16. SECURITY CLASSIFICATION OF:</b>			<b>17. LIMITATION OF ABSTRACT</b>  UU	<b>18. NUMBER OF PAGES</b>  50	<b>19a. NAME OF RESPONSIBLE PERSON</b> Frank Fresconi
<b>a. REPORT</b> Unclassified	<b>b. ABSTRACT</b> Unclassified	<b>c. THIS PAGE</b> Unclassified			<b>19b. TELEPHONE NUMBER (Include area code)</b> 410-306-0794

---

## Contents

---

<b>List of Figures</b>	<b>iv</b>
<b>List of Tables</b>	<b>vi</b>
<b>1. Introduction</b>	<b>1</b>
<b>2. Concept</b>	<b>2</b>
<b>3. Aerodynamic Characterization</b>	<b>4</b>
<b>4. Aerodynamic Model</b>	<b>22</b>
<b>5. Flight Mechanics</b>	<b>24</b>
<b>6. Delivery in the Ballistic Environment</b>	<b>25</b>
<b>7. Delivery Characterization</b>	<b>27</b>
<b>8. Conclusions</b>	<b>36</b>
<b>9. References</b>	<b>37</b>
<b>List of Symbols, Abbreviations, and Acronyms</b>	<b>40</b>
<b>Distribution List</b>	<b>41</b>

---

## List of Figures

---

Figure 1. Rotating wing maneuver concept. ....	2
Figure 2. Snapshots (viewed from base in earth-fixed reference frame) over one revolution of rotating wing maneuver concept with two actuators. ....	3
Figure 3. Projectile geometry (dimensions in calibers). ....	4
Figure 4. Wing geometry. ....	5
Figure 5. Body-fixed coordinate system and aerodynamic angles. ....	6
Figure 6. Instrumented model mounted in WT facility test section. ....	7
Figure 7. Stowed roll angle (left-to-right: 0, 30, 60, and 90 deg). ....	9
Figure 8. Normal force coefficient for different airfoils. ....	9
Figure 9. Pitching moment coefficient for different airfoils. ....	10
Figure 10. Normal force coefficient for different deflections. ....	11
Figure 11. Pitching moment coefficient for different deflections. ....	11
Figure 12. Representative CFD model configurations. ....	14
Figure 13. Computational mesh on symmetry plane and projectile surfaces. ....	15
Figure 14. Mach number contours on vertical symmetry plane at $\alpha = 0$ deg. ....	16
Figure 15. Close-up view of Mach number contours on vertical symmetry plane at $\alpha = 0$ deg, actuator deflections of 4, 6, 8, and 10 deg. ....	16
Figure 16. Comparison of CFD and WT data for body alone (configuration 1): (a) axial force, (b) forebody axial force, (c) normal force, and (d) pitching moment. ....	17
Figure 17. Comparison of CFD and WT data for configuration 11120: (a) axial force, (b) forebody axial force, (c) normal force, and (d) pitching moment. ....	18
Figure 18. Axial force coefficient for projectile body. ....	20
Figure 19. Normal force coefficient for control. ....	20
Figure 20. Earth and body-fixed coordinate systems and Euler angles. ....	24
Figure 21. Horizontal plane ballistic burst points. ....	28
Figure 22. Vertical plane ballistic burst points. ....	28
Figure 23. Ground plane control authority for airfoil parameter. ....	29
Figure 24. Control authority for airfoil parameter. ....	30
Figure 25. Control authority for planform parameter. ....	31
Figure 26. Control authority for deflection parameter. ....	31
Figure 27. Control authority for standoff parameter. ....	32
Figure 28. Control authority for number of wings. ....	32

Figure 29. Pitch angle-of-attack for maneuver up. ....	33
Figure 30. Yaw angle-of-attack for maneuver up. ....	34
Figure 31. Spin rate for maneuver up. ....	34
Figure 32. Mach number for maneuver up. ....	35
Figure 33. Vertical plane trajectory for maneuver up.....	35

---

## List of Tables

---

Table 1. WT matrix key.....	8
Table 2. WT matrix.....	8
Table 3. Aerodynamics from WT for all configurations. ....	12
Table 4. Aerodynamics from WT for configuration 11120 for all stowed roll angles. ....	12
Table 5. Projectile aerodynamics.....	20
Table 6. Projectile magnus aerodynamics. ....	21
Table 7. Control aerodynamics for all stowed roll angles. ....	21
Table 8. Models and data for man portable delivery process. ....	27

---

## 1. Introduction

---

Improving delivery accuracy of squad-level weapons is the motivation for this report. Guiding projectiles is a means of compensating for delivery errors due to effects such as wind, weapon aiming, or muzzle velocity variation. Maneuvering projectile flight is a critical element of any guidance technology. The focus of this report is maneuvering small-diameter projectiles.

Guns are often rifled to impart spin to projectiles, which results in gyroscopic stability (1, 2). One advantage of spin-stabilized projectiles over fin-stabilized projectiles is reduced drag. Flight stability of controlled, spin-stabilized projectiles, however, is more complex than ballistic flight stability (3, 4). Maneuvers directed perpendicular to the gravity vector increase the chance for unstable flight. Additionally, high-spin rate complicates the actuation technology (e.g., higher bandwidth requirements). Portions of the projectile or the control mechanism may be decoupled from the main projectile body to mitigate these issues (5–9). In contrast to fin-stabilized projectiles, the optimal placement for maneuverability of spin-stabilized projectiles is at the rear of the body due to the center-of-pressure location (10, 11).

The launch velocity of man portable systems is often limited by weapon recoil. There is a maximum acceptable impulse of the launch event on the shoulder of the Soldier. Low-launch velocity translates to low-dynamic pressure available for maneuvering an aerodynamic control mechanism. Thrusters, nonaerodynamic in nature, are viable options in low-dynamic pressure flight regimes (12–17). The angular motion of the projectile induced by impulsive maneuvers may be deleterious to seeker-based guidance performance. Current flow control technologies feature limited control authority (18).

The size, weight, power, and cost requirements for the maneuver technologies in small-diameter projectiles are challenging. Man portable weapons, from assault rifles to grenade launchers, shoulder fired weapons, and mortars are often about 80 mm in diameter or smaller. Actuators, sensors, electronics, embedded processors, and a power source must fit along with other potential subsystems such as fuzing and warhead. Current fin or canard actuation technologies are difficult to package in less than 80-mm-diameter projectiles (19–22).

The high-structural loads applied to these components during gun launch impose severe constraints (23, 24). Reducing the size and number of moving parts, as well as properly supporting components, is often necessary for ensuring survivability and reliability in the gun-launched environment.

The goal of this report is to explore the aeromechanics of a small guided projectile concept to assess the efficacy in improving delivery accuracy. A rotating wing actuator is the basis of this new maneuver concept. The novel contributions are the flight concept, theoretical modeling of the concept, computational and experimental aerodynamic characterization, and assessment of control authority with respect to ballistic dispersion.

This report first outlines the maneuver concept and geometry of the projectile and control parameters. Next, aerodynamic data obtained through experimental and computational techniques are provided. Aerodynamics were used in a model as input to the flight mechanics. Lastly, launch and flight system simulations are shown which quantify the ballistic dispersion, guided flight stability and control authority.

---

## 2. Concept

---

The maneuver concept, shown in the figure 1, applies to spin-stabilized projectiles. A wing-shaped actuator aligned with the spin axis of the projectile is used to constantly rotate an aerodynamic surface, such as a miniature wing, with respect to the projectile body. Over one revolution of projectile spin the actuator rotates the aerodynamic surface or wing from exposed to the airstream (effecting lateral maneuver as shown in figure 1) to stowed internally within the projectile body. Rotating the aerodynamic surface opposite the projectile spin achieves a consistent maneuver direction. Phase shifting the wing rotation with respect to the projectile rotation changes the maneuver direction.

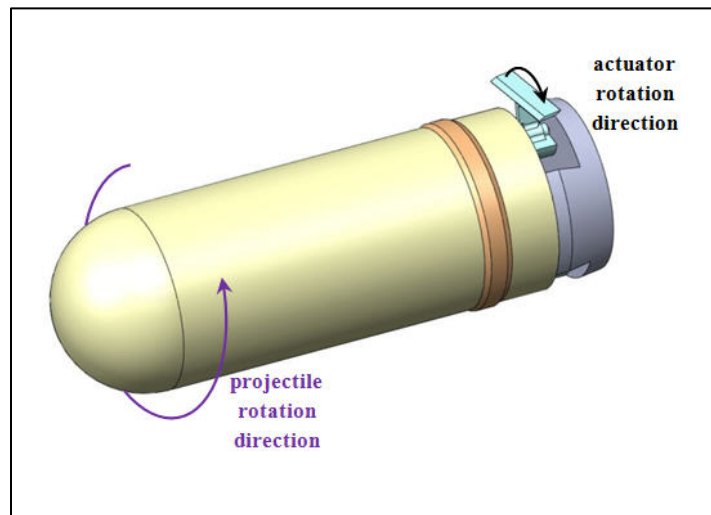


Figure 1. Rotating wing maneuver concept.

Further pictorial description of the maneuver concept is provided in figure 2. A complete revolution of spin advances in 45-deg roll-angle increments in a counter-clockwise manner around the figure. A two-actuator variant, viewed from the base of the projectile in an Earth-fixed frame, is illustrated. The projectile rotates in the clockwise direction and the actuation assembly rotates in the counter-clockwise direction. Each successive rendering illustrates the manner in which the rotational actuator exposes the wing to the airstream to produce a lateral maneuver.

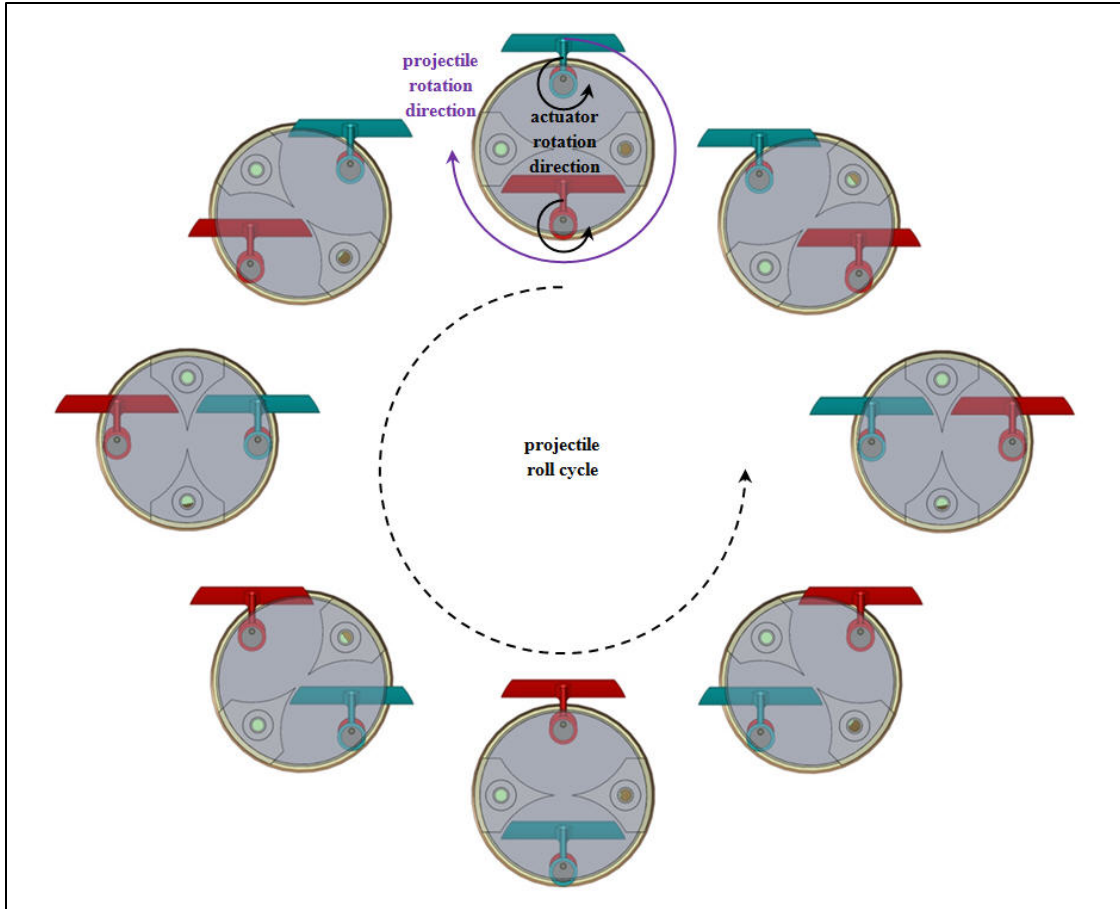


Figure 2. Snapshots (viewed from base in earth-fixed reference frame) over one revolution of rotating wing maneuver concept with two actuators.

This maneuver concept contrasts with conventional aerodynamic surface actuation technologies wherein rotational actuators travel less than one full rotation (e.g., servomechanisms) to deflect aerodynamic surfaces. Linear actuation techniques are not as attractive in the high-spin rate environment due to the power requirements (25, 26). The approach outlined in this report marries low-cost actuation technology with spin-stabilized flight dynamics for a novel solution. Rotational actuators with spin rates in the 10–1000-Hz range are commercially available in high volume at low cost with small size, weight, and power characteristics. Companion efforts are investigating the mechatronics, control, and performance of the maneuver technology (27).

---

### 3. Aerodynamic Characterization

---

The projectile geometry is presented in figure 3. A hemispheric nose, adequate for subsonic flight, is followed by a 2.25-caliber (cal.) cylindrical section prior to a 7-deg boattail for wake drag reduction. The engraving band was 0.125 cal. long and 0.02875 cal. in height. The specifics of this configuration were chosen based on an analysis of subsystem requirements to maximize range considering the following launch and flight characteristics: caliber, projectile length-to-diameter ratio, stabilization method, recoil impulse, and propulsion (gun or gun and rocket) (28). A center-of-gravity location 1.675 cal. from the nose was used for all calculations.

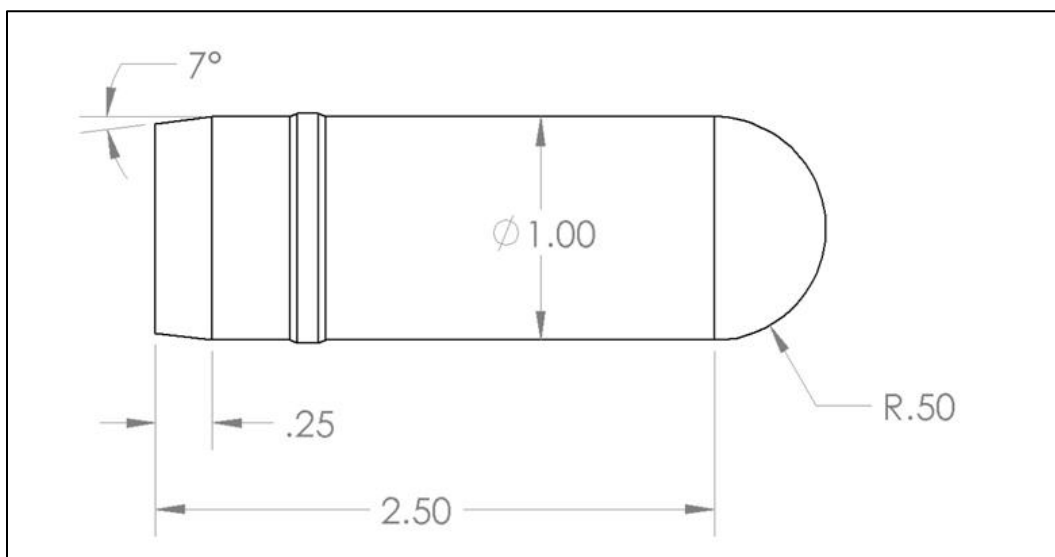


Figure 3. Projectile geometry (dimensions in calibers).

A parametric analysis of the wing was conducted to define optimal characteristics. The parameters under investigation were the chord ( $C$ ), span ( $S$ ), deflection angle ( $\delta$ ), airfoil profile, and stand-off from the projectile body ( $H$ ). The geometry for the wing is provided in figure 4.

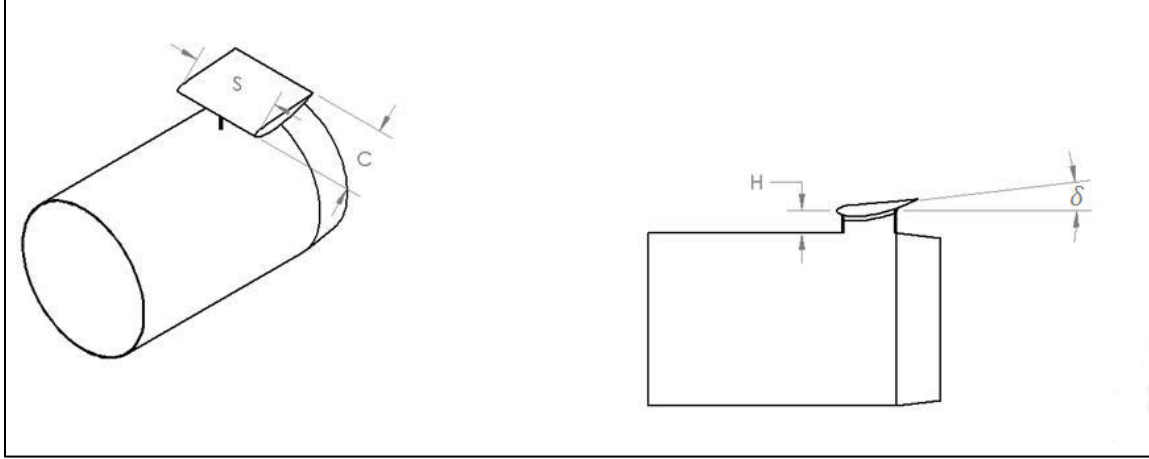


Figure 4. Wing geometry.

A comprehensive aerodynamic characterization of the projectile and wing were undertaken. The approach was to initially perform semiempirical aeroprediction (SEAP) in the Projectile, Rockets, and Ordnance Design and Analysis System (PRODAS) Spinner code on the projectile body (29). Projectile and wing static aerodynamic data were collected during wind tunnel (WT) experiments. These data served to identify optimal wing characteristics and validate computational fluid dynamics (CFD) predictions. Modeling down-selected geometries and performing CFD provided dynamic derivatives and, along with the WT data, enabled the aerodynamic model to be formulated. Characterizations were performed of the projectile body and of the projectile body with the wing. To isolate the maneuver aerodynamics, projectile body aerodynamic data were subtracted from the projectile body with wing data. Thus, wing and any wing-body interference effects were modeled as part of the maneuver aerodynamics.

The body-fixed coordinate system, defined in the figure 5, was used to quantify aerodynamics. The coordinate axes, and subsequently the velocity, forces, and moments, follows the right-hand rule. Aerodynamic angles (pitch angle-of-attack,  $\alpha$ , yaw angle-of-attack,  $\beta$ , total angle-of-attack,  $\bar{\alpha}$ , and aerodynamic roll angle,  $\phi_A$ ) are computed based on the body-fixed velocity components ( $[u \ v \ w]^T$ ).

$$\begin{aligned}
 \alpha &= \text{asin} \left[ \frac{w}{\sqrt{u^2 + w^2}} \right] \\
 \beta &= \text{asin} \left[ \frac{v}{\sqrt{u^2 + v^2 + w^2}} \right] \\
 \bar{\alpha} &= \text{asin} \left[ \frac{\sqrt{v^2 + w^2}}{\sqrt{u^2 + v^2 + w^2}} \right] \\
 \phi_A &= \text{atan} \left( \frac{v}{w} \right)
 \end{aligned} \tag{1}$$

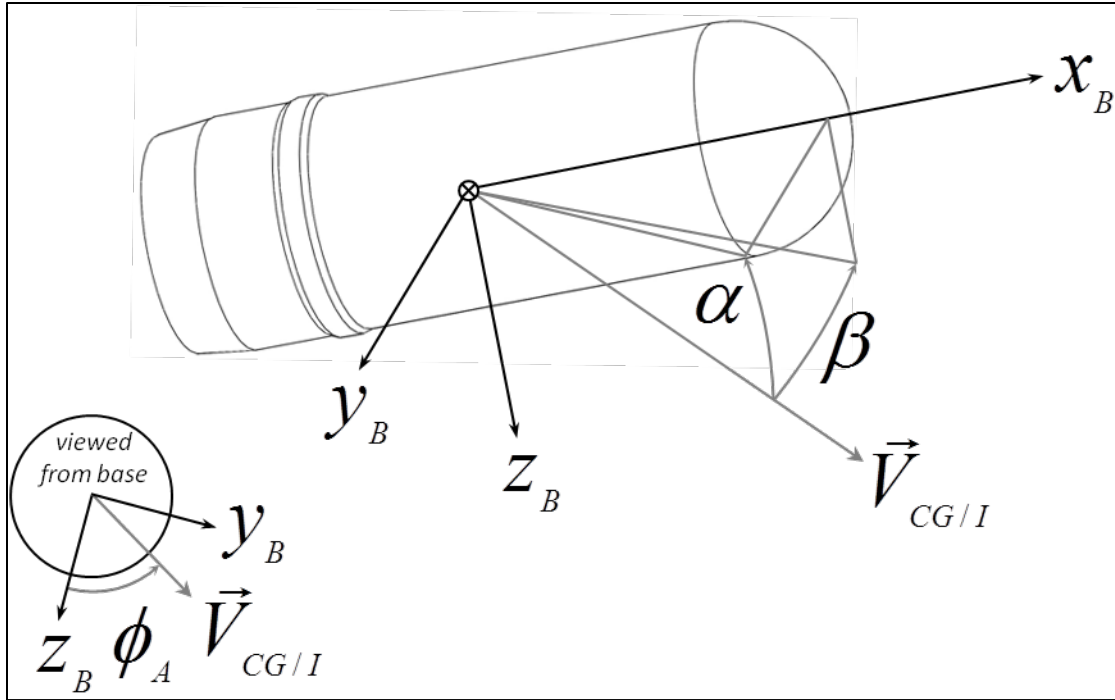


Figure 5. Body-fixed coordinate system and aerodynamic angles.

Subsonic experiments were conducted in a blow-down WT with a 28 in high  $\times$  40 in wide test section housed at the Edgewood Area of Aberdeen Proving Ground, MD. Models were constructed with rapid-prototyping tools. The projectile diameter was 70 mm and was made from polycarbonate with fused deposition modeling. The wings were made from Somos Nanotool with stereolithography. The models were mounted on a sting with a 3/8-in-diameter five component balance (Modern Machine & Tool Co.). The balance featured sensitivities of 10 lb for axial force, 8 lb for normal force, 5 lb for side force, and 8 in-lb for pitching moment and side moment. An image of the model with balance on the sting in the tunnel is shown in figure 6.

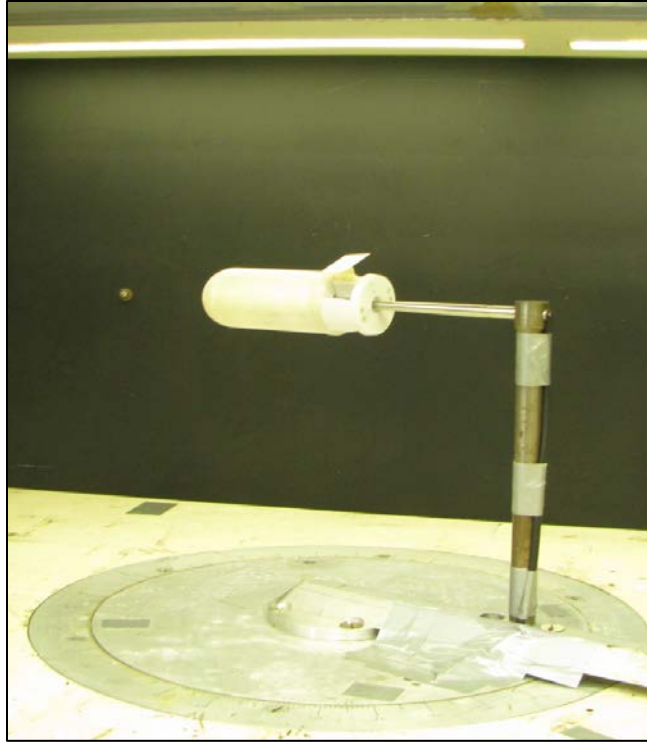


Figure 6. Instrumented model mounted in WT facility test section.

Data were obtained in the WT at angles-of-attack of  $\pm 12$  deg in 1- or 2-deg increments. The Mach number was approximately 0.2 since this is of tactical interest for low-velocity grenade weapons (30). The WT key and matrix is given in tables 1 and 2. Two bodies were examined; the first was a replica of the projectile geometry outlined in figure 3 and the second was a similar body with a cavity to accommodate the wing. The effect of airfoil camber was investigated along with planform. The wing deflection angle was studied to assess stall. Standoff of the wing from the projectile body was varied. The effectiveness of the wing as a function of the amount of wing exposed to the airstream, or stowed roll angle ( $\hat{\phi}$ , measure of amount of control surface exposed to airstream) was obtained. The stowed roll angle can be visualized in figure 7. Here, the decrease in the wing area exposed to the airstream as stowed roll angle increases from 0 to 90 deg in 30-deg increments can be seen with the model in the WT. When describing a particular configuration the format will be to concatenate the identification number for successive parameters in the WT key. For example, configuration 11120 is the projectile with cavity, NACA\* 4415 airfoil, 0.48-cal. chord  $\times$  0.61-cal. span, and 8-deg deflection. Data were also collected at aerodynamic roll angles of 0, 22.5, 45, 67.5, and 90 deg.

---

\*National Advisory Committee for Aeronautics.

Table 1. WT matrix key.

Parameter	Identification No.	Description
Body	0	Projectile body
	1	Projectile body with cavity
Airfoil	0	NACA 0015
	1	NACA 4415
Planform	0	0.61-cal. chord $\times$ 0.61-cal. span
	1	0.48-cal. chord $\times$ 0.61-cal. span
	2	0.32-cal. chord $\times$ 0.61-cal. span
	3	0.48-cal. chord $\times$ 0.48-cal. span
	4	0.32-cal. chord $\times$ 0.48-cal. span
Deflection	0	4 deg
	1	6 deg
	2	8 deg
	3	10 deg
Standoff	0	5.28 mm from body outer diameter
	1	0.3 mm from body outer diameter
Stowed roll angle	0	0 deg
	1	30 deg
	2	60 deg
	3	90 deg
Aerodynamic roll angle	0	0 deg
	1	22.5 deg
	2	45 deg
	3	67.5 deg
	4	90 deg
	5	60 deg
	6	30 deg

Table 2. WT matrix.

Body	Airfoil	Planform	Deflection	Standoff	Stowed Roll	Aero Roll
0	NA	NA	NA	NA	NA	NA
1	NA	NA	NA	NA	NA	0
1	1	1	2	0	0	0
1	0	1	2	0	0	0
1	1	2	2	0	0	0
1	1	3	2	0	0	0
1	1	4	2	0	0	0
1	1	1	0	0	0	0
1	1	1	1	0	0	0
1	1	1	3	0	0	0
1	1	1	2	1	0	0
1	1	1	2	0	0	1
1	1	1	2	0	0	2
1	1	1	2	0	0	3
1	1	1	2	0	0	4
1	NA	NA	NA	NA	NA	4
1	1	1	2	0	1	5
1	1	1	2	0	2	6
1	1	1	2	0	3	0
0	NA	NA	NA	NA	NA	NA

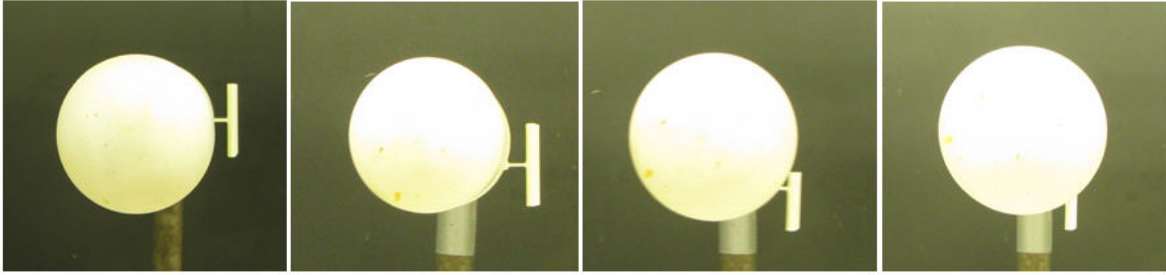


Figure 7. Stowed roll angle (left-to-right: 0, 30, 60, and 90 deg).

Data collected at discrete angles-of-attack were inspected and least-squares fit with an appropriate polynomial expansion in angle-of-attack. Some examples of WT data and subsequent polynomial fits are shown. The fits for body-wing and body alone were subtracted as described earlier to isolate the control effects. Figure 8 shows the normal force coefficient for different airfoils. The projectile body data and fit are in black. The NACA 0012 data are in blue and the NACA 4412 data are purple. Points represent WT data and curves represent fits. Solid lines represent the control force and moment obtained by subtracting the body-wing from the body-alone data. As expected, the body-alone data goes through the origin. When adding the aerodynamic asymmetry of the deflected wing, however, a trim force and change in nonlinearity with angle-of-attack emerges. These data show that adding camber increases the effectiveness of the control by almost a factor of 2 in the trim force.

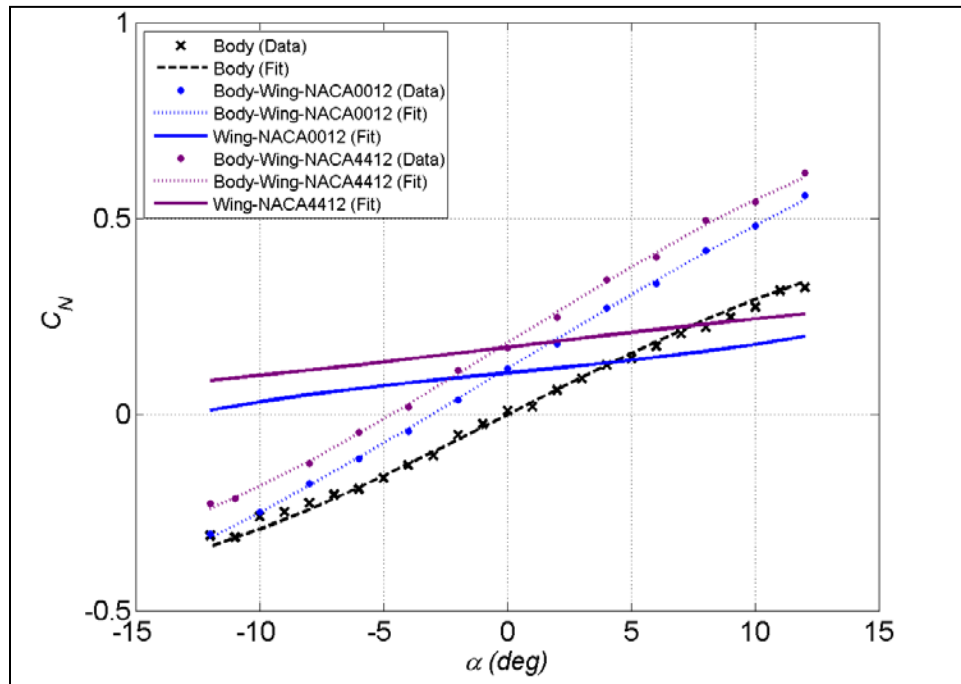


Figure 8. Normal force coefficient for different airfoils.

The pitching moment for various airfoils is given in figure 9. Again, the body-alone data goes through the origin. The slope of the body data is positive since the projectile is statically unstable. Addition of the wing greatly changes the nonlinearity and again features a nonzero intercept. Pitching moment for the NACA 4412 indicates a greater trim moment, which results in more control authority.

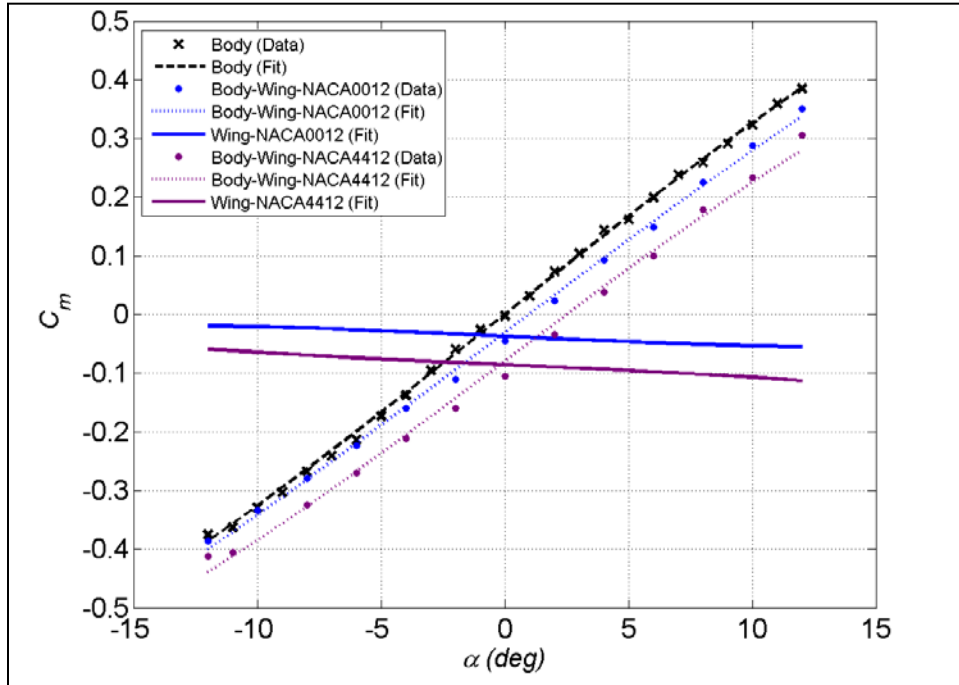


Figure 9. Pitching moment coefficient for different airfoils.

Figures 10 and 11 provide the normal force and pitching moment for the various deflection angles. Trends are similar to those described for the airfoil parameter. Addition of the wing induces a trim force and moment and change to the nonlinearity with angle-of-attack. The wing effectiveness increases with deflection angle since the lift on a wing, scales with effective angle-of-attack (projectile body and deflection angle combined). Stall on the wing does not appear significant even for effective angles-of-attack greater than 12 deg.

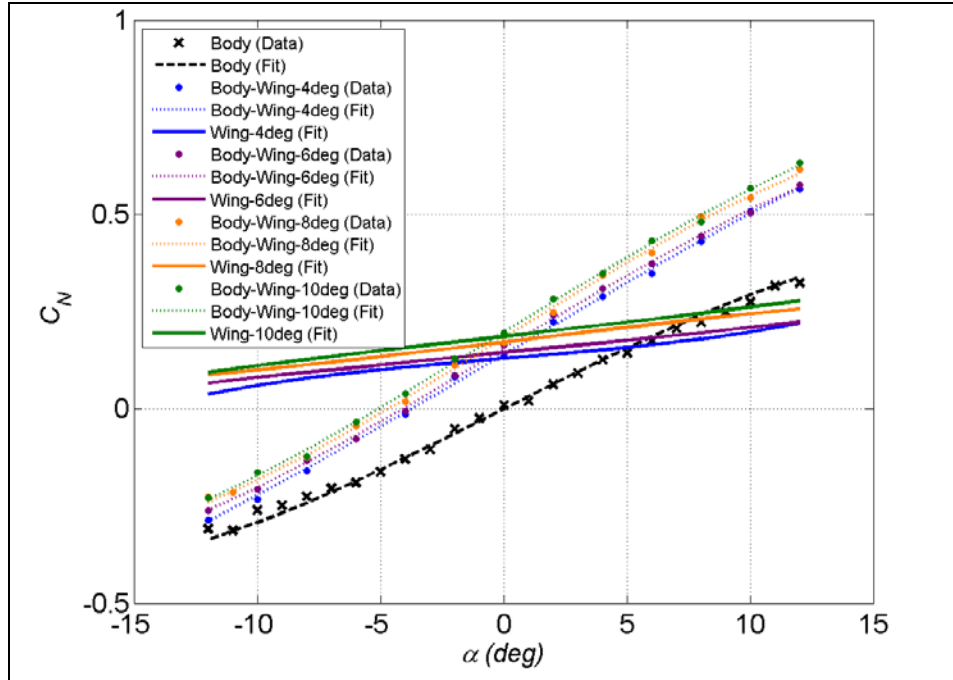


Figure 10. Normal force coefficient for different deflections.

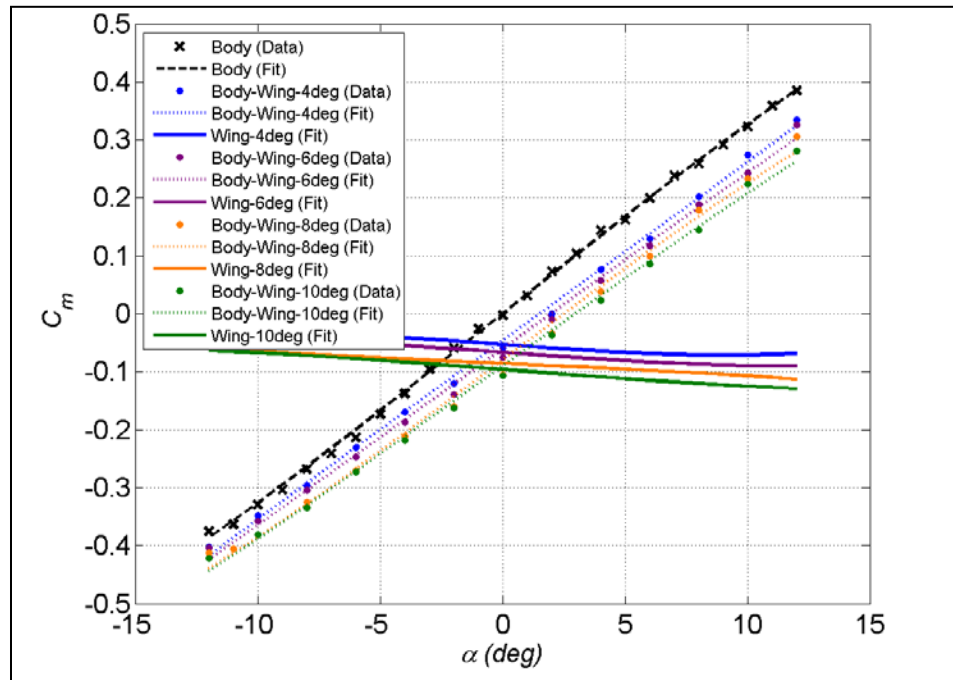


Figure 11. Pitching moment coefficient for different deflections.

The aerodynamic data for all configurations from WT experiments is compiled in table 3. In general, the wing increases drag while also providing the necessary normal force for maneuver. The cambered airfoil outperforms the airfoil without camber. Larger planform increases effectiveness. Control effectiveness increased with deflection, although the results at 10 deg were not appreciably higher than those at 8 deg. The larger standoff distance was critical to getting the flow around the wing sufficiently separate from the flow near the projectile.

Table 3. Aerodynamics from WT for all configurations.

Configuration	$C_{X_0}$	$C_{X_{\alpha^2}}$	$C_{N_0}$	$C_{N_{\alpha}}$	$C_{N_{\alpha^3}}$	$C_{m_0}$	$C_{m_{\alpha}}$	$C_{m_{\alpha^3}}$
0	0.169782	1.011851	0.010264	1.829601	-4.94869	0.005764	1.932517	-1.99989
11120	0.070048	0.2794	0.172031	0.437611	-0.75652	-0.08572	-0.10841	-0.44945
10120	0.03475	0.474122	0.106159	0.35477	2.114011	-0.03716	-0.11304	0.665462
11220	0.030063	0.393898	0.112284	0.311331	-0.09466	-0.05199	-0.06694	-0.21999
11320	0.036989	0.367927	0.120833	0.199218	3.137703	-0.05406	-0.10749	2.116242
11420	0.019322	0.26236	0.071913	0.011366	4.718838	-0.02909	-0.07454	2.58084
11100	0.042328	0.386538	0.129257	0.304703	3.014388	-0.05265	-0.17627	2.30084
11110	0.054294	0.155404	0.14464	0.36058	0.283997	-0.06663	-0.17575	1.483676
11130	0.075184	0.223102	0.186378	0.415412	0.537722	-0.09615	-0.18314	0.603045
11121	0.042328	0.386538	0.129257	0.304703	3.014388	-0.05265	-0.17627	2.30084

The effect of stowed roll angle is demonstrated in table 4. As less of the wing is exposed to the airstream, the drag, lift, and moment decrease. The wing effectiveness does not fall sharply with stowed roll angle; however, since this concept is able to keep appreciable wing in the freestream even at higher stowed roll angles as seen in figure 7. A roll torque is expected to be imparted to the projectile during the partially stowed stages of the cycle; however, roll moments were not measured in the WT. Roll moments were evaluated via CFD and discussed in the following.

Table 4. Aerodynamics from WT for configuration 11120 for all stowed roll angles.

$\hat{\phi}$ ,	$C_{X_0}$	$C_{X_{\alpha^2}}$	$C_{N_0}$	$C_{N_{\alpha}}$	$C_{N_{\alpha^3}}$	$C_{m_0}$	$C_{m_{\alpha}}$	$C_{m_{\alpha^3}}$
0 deg	0.070048	0.2794	0.172031	0.437611	-0.75652	-0.08572	-0.10841	-0.44945
30 deg	0.059063	0.038751	0.151855	0.427696	0.636527	-0.09272	-0.22951	0.171845
60 deg	0.026487	-0.0745	0.07989	0.436496	2.563468	-0.06165	-0.20457	0.082161
90 deg	0.024284	-0.19	0.055608	0.299621	5.386849	-0.04791	-0.30041	0.262917

The CFD aerodynamics characterization (31) consisted of a WT validation series and a down-selected concept characterization series. Configuration 11120 was the down-selected concept for the remainder of the CFD analysis due to its attractive characteristics based on the WT experiments.

The CFD characterization was performed using the commercially available CFD<sup>++</sup> code, version 12.1 (32). CFD<sup>++</sup> solves the three-dimensional, compressible Reynolds-Averaged Navier-Stokes (RANS) equations using a finite volume method. The inviscid flux function was a second-order,

upwind scheme using a Harten-Lax-Van Leer-Contact (HLLC) Riemann solver and a multidimensional Total-Variation-Diminishing (TVD) continuous flux limiter (32). The solution is advanced to steady-state using a point-implicit time integration scheme with local time stepping and multigrid convergence acceleration. The low-speed preconditioning version of the compressible solver was used, as it is appropriate for Mach numbers less than about 0.3. CFD<sup>++</sup> has many common turbulence models available. Menter's Shear Stress Transport (SST) model (33) was chosen for this study based on some initial comparisons with predictions using the realizable  $k-\varepsilon$  model (34) and the WT data for one body-alone configuration. Simulations were performed primarily on the SGI ICE X System (SPIRIT) located at the U.S. Air Force Research Laboratory (AFRL) Department of Defense (DOD) Supercomputing Resource Center (DSRC) at Wright-Patterson Air Force Base, OH. Simulations were also undertaken on the Cray XE6 (GARNET) located at the U.S. Army Engineering Research and Development Center (ERDC) DSRC in Vicksburg, MS, and the IBM iDataPlex (PERSHING) located at the U.S. Army Research Laboratory (ARL) DSRC at Aberdeen Proving Ground, MD.

The first phase of the CFD characterization was a validation series consisting of selected configurations tested in the WT. The Mach number was 0.2 and the WT model was 1.75 scale (70 mm). Figure 12 shows several of the configurations that were simulated. CFD characterization was performed for the solid body alone, the body alone with empty actuator cavity, and the body with actuator wing deflections of 4, 6, 8, and 10 deg. CFD predictions for configuration 11120 actuator wing were performed for aerodynamic roll angles of 22.5, 45, 67.5, and 90 deg, in addition to the 0 deg configuration shown in figure 12. Several cases with part of the WT sting modeled were investigated to determine if there were sting effects present. The WT walls were not modeled. All simulations were performed with the actuator wing at a fixed, fully deployed orientation.

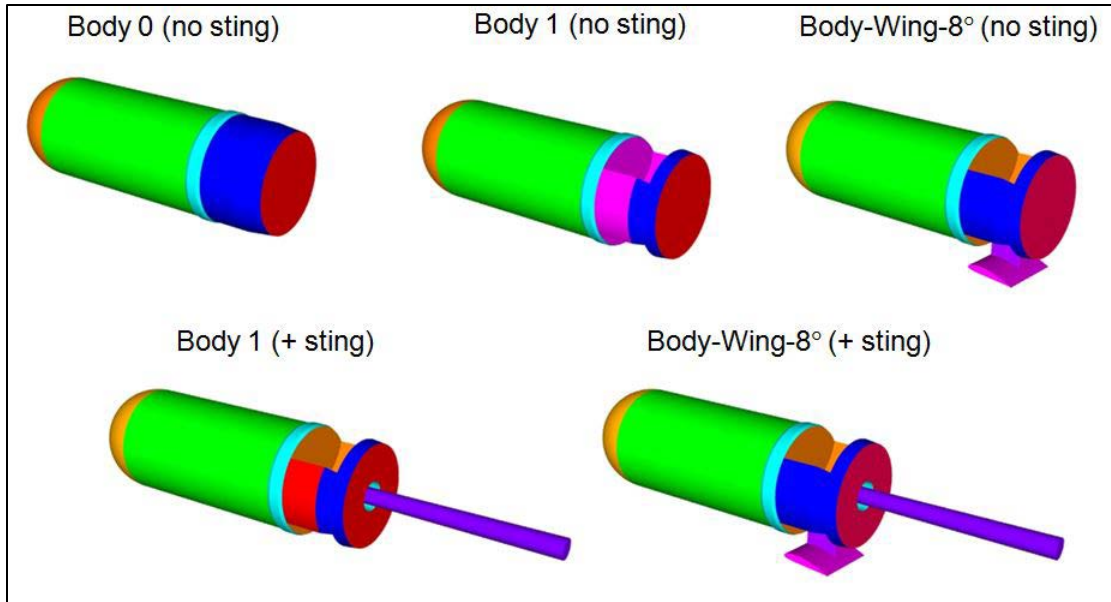


Figure 12. Representative CFD model configurations.

The computational domain was a sphere with an outer boundary located 50 cal. from the projectile. Figure 13 shows some views of the mesh on the symmetry plane of the computational domain and the projectile surfaces. The mesh was made using MIME version 4.1, (35) an unstructured mesh generator using tetrahedral, prism, and pyramidal cells. The mesh sizes were 9.6, 11.5, and 19.7 million cells for the solid body alone, body alone with empty actuator cavity, and body with the actuator, respectively. The results show some effect of the sting on the axial force. Therefore, the validation simulations were performed with the sting (and at 1.75 scale), while the concept characterization simulations were performed with the unscaled projectile model with no sting.

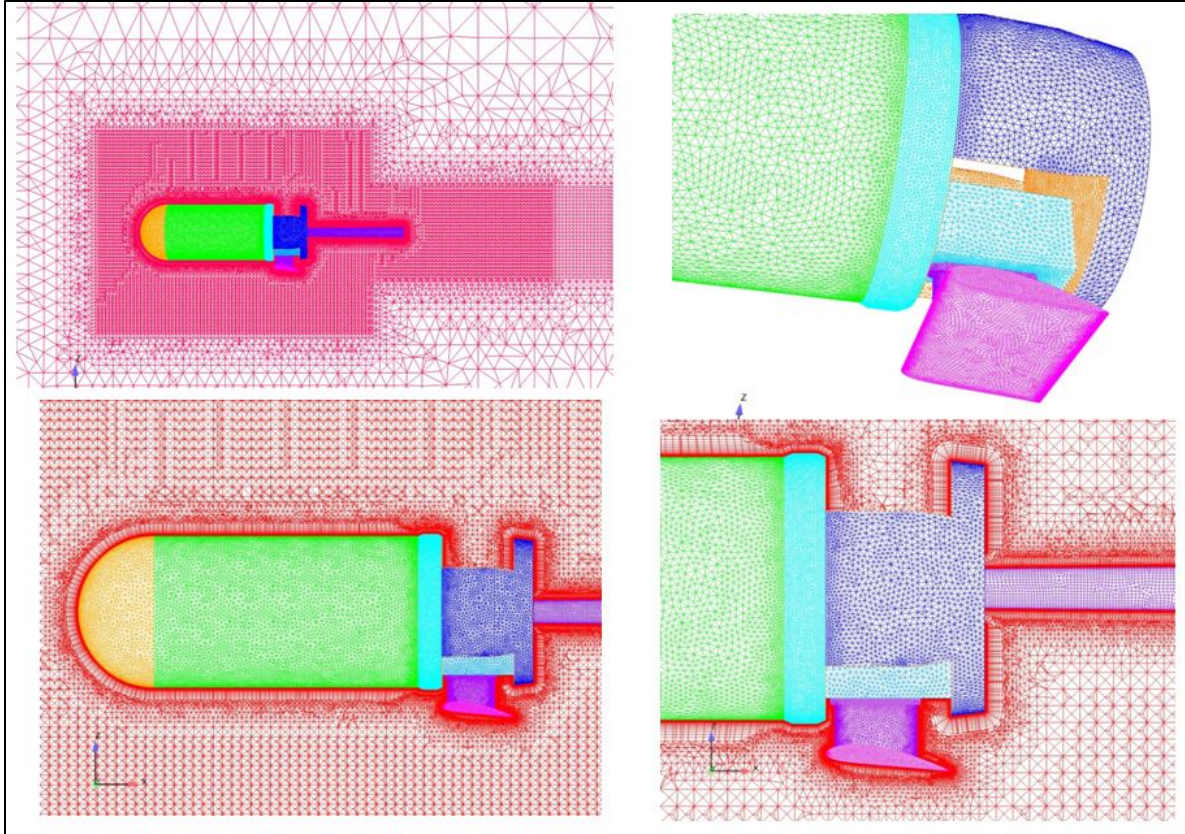


Figure 13. Computational mesh on symmetry plane and projectile surfaces.

Validation simulations were performed at  $-12 \text{ deg} \leq \alpha \leq 12 \text{ deg}$  in 2-deg increments at Mach 0.2 at standard temperature and pressure (288.15 K and 101.325 kPa, respectively). The data from the discrete angles-of-attack were then least-squares fit with an appropriate polynomial expansion in angle-of-attack. All simulations were steady-state. Figure 14 shows some typical flowfield visualization results, including the effect of the sting on the base flow. The wing actuator has a pronounced effect on the base flow and the sting has a small effect on the base flow. Figure 15 shows a close-up view of the actuator region for the four actuator wing deflections considered. Qualitatively, there is not much difference in the flowfields, but as shown in figure 10, the normal force scales with wing deflection. It must be noted that these flowfields are forced to a steady-state by the solution technique. These flowfields are most likely highly unsteady, but since the rotation of the actuator in this stage is not included, the steady-state solution is adequate.

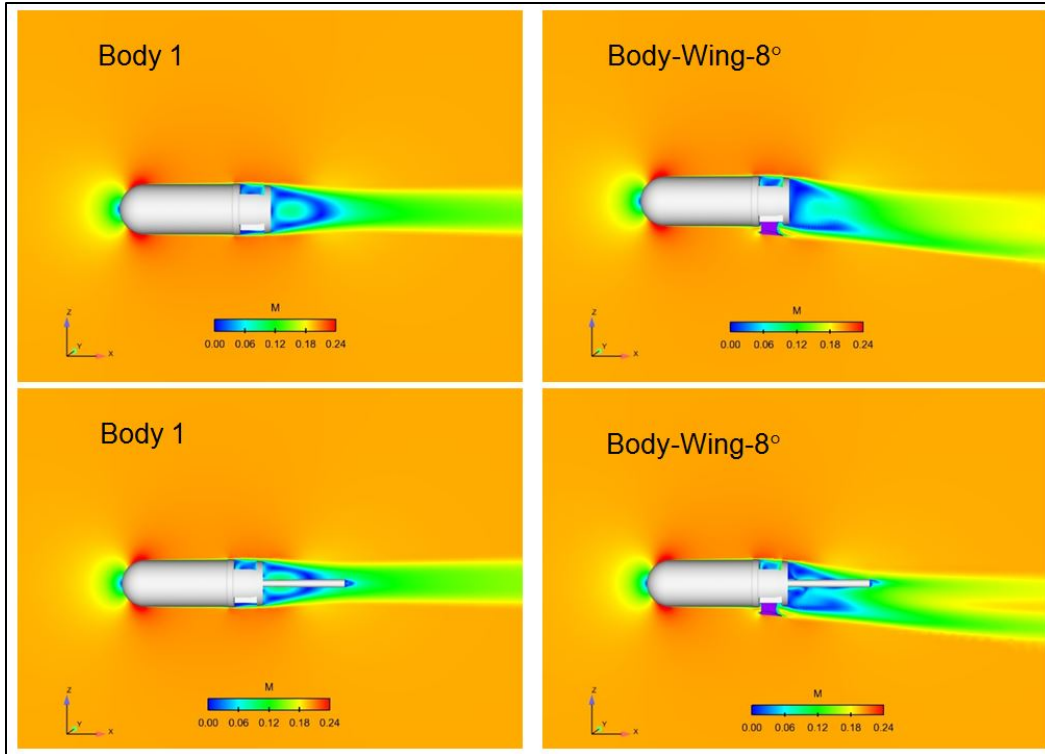


Figure 14. Mach number contours on vertical symmetry plane at  $\alpha = 0$  deg.

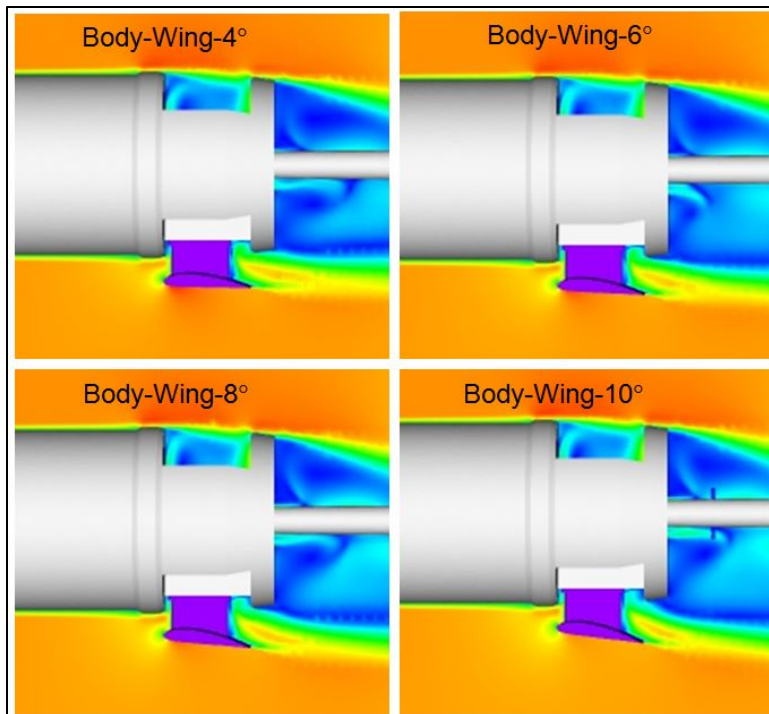


Figure 15. Close-up view of Mach number contours on vertical symmetry plane at  $\alpha = 0$  deg, actuator deflections of 4, 6, 8, and 10 deg.

Figure 16 shows the comparison of CFD with WT data for the body-alone configuration with the empty actuator cavity. Figure 16a shows the total axial force, for which the data compare reasonably well at  $\alpha = 0$  deg. The case without the sting shows a larger increase in axial force than observed in the WT data as the projectile deflection increases or decreases. The case with the sting, however, compares very well with the WT data at positive angles-of-attack and much better than the case without the sting at negative angles. Figure 16b shows the forebody axial force, i.e., the axial force on all surfaces except the projectile base. The two CFD results nearly overlay, indicating the differences are all on the projectile base and due to the sting effects. Figures 16b and 16c present the normal force and pitching moment results, respectively, and indicate that there are no sting effects on these parameters. The normal force compares very well to the experimental data while the predicted pitching moment slope is slightly higher than observed in the WT. The latter can possibly be due to a laminar-to-turbulent transition in the WT that is not accounted for in the CFD, which is assumed completely turbulent.

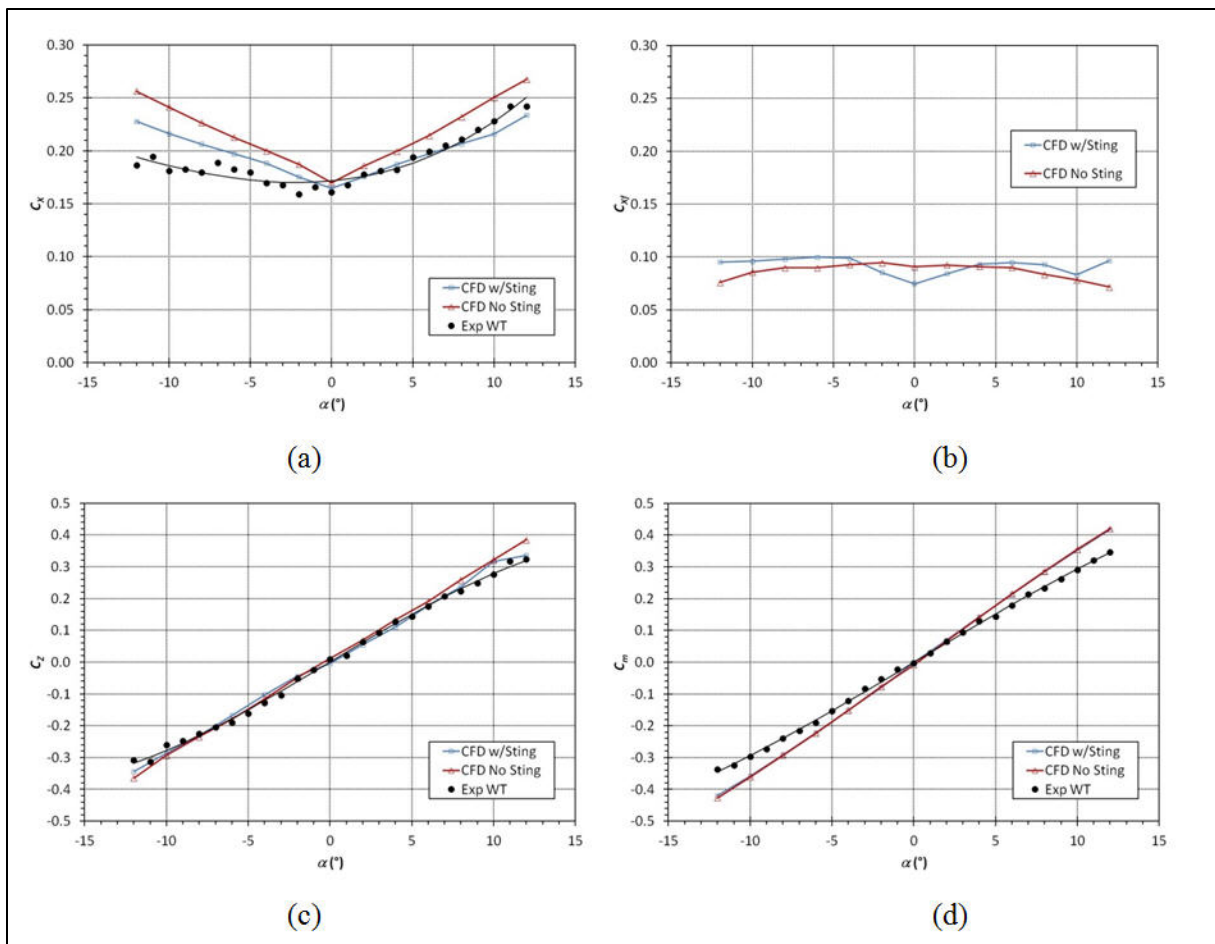


Figure 16. Comparison of CFD and WT data for body alone (configuration 1): (a) axial force, (b) forebody axial force, (c) normal force, and (d) pitching moment.

Figure 17 shows the comparison of CFD with WT data for the 11120 configuration. From the axial force plots (figures 17a and 17b), it can be seen that sting effects are only observed at  $\alpha > 2$  deg. Also, some sting effects can now be observed on the pitching moment (figure 16d) for  $\alpha > 5$  deg as indicated by the separation of the two CFD results. The normal force (figure 16c) is also over predicted for  $\alpha > -4$  deg. The experimental uncertainty and comparison with CFD indicates that the CFD results can be applied with confidence for a comprehensive characterization of the concept.

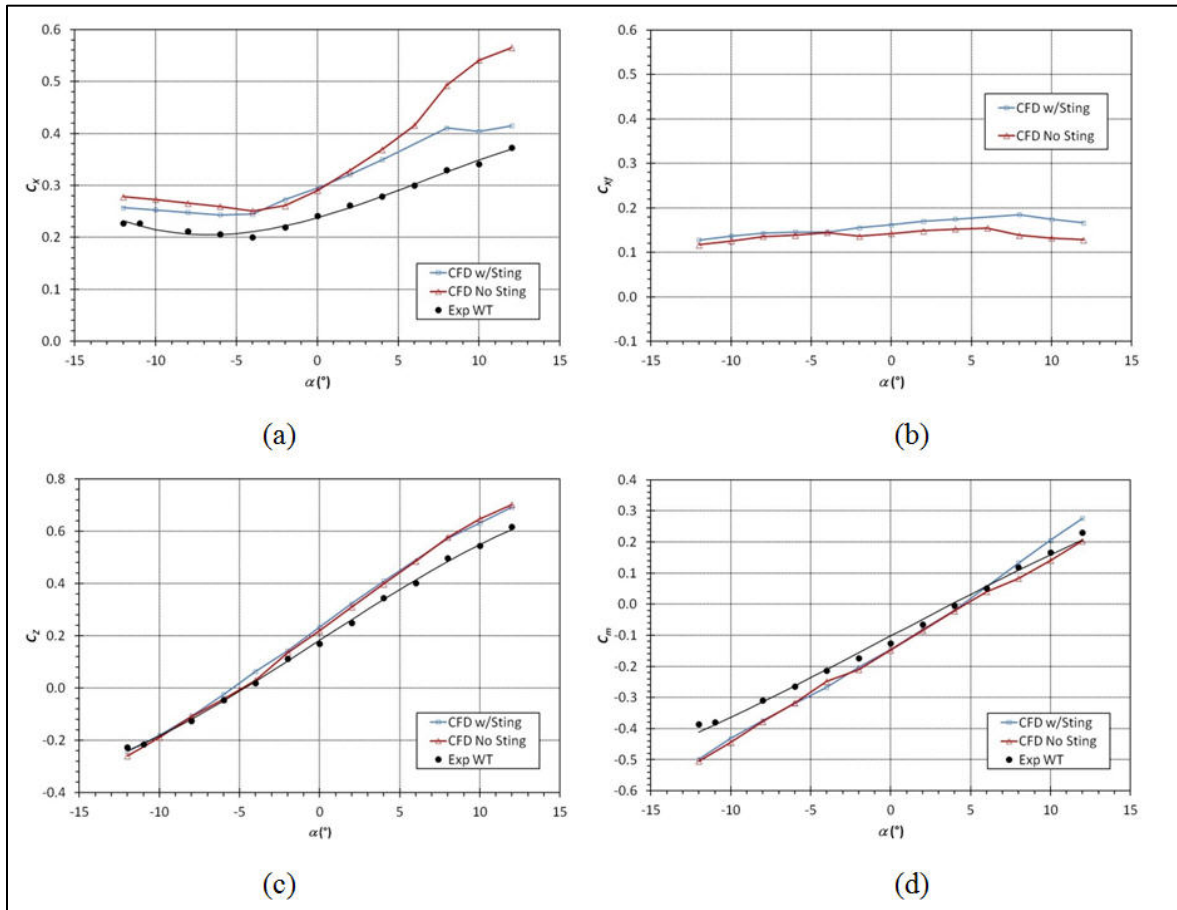


Figure 17. Comparison of CFD and WT data for configuration 11120: (a) axial force, (b) forebody axial force, (c) normal force, and (d) pitching moment.

The purpose of the concept assessment phase of the CFD study was to determine the dynamic derivatives, i.e., Magnus, roll-damping, and pitch-damping moments on the down-selected configuration (11120). The scale of the projectile in this phase of the study was 40 mm, so the mesh was scaled down appropriately. Roll-damping and Magnus moments were generated by performing unsteady simulations of the projectile rolling at the nominal spin rate (54.2 Hz) at angles-of-attack  $-12 \text{ deg} \leq \alpha \leq 12 \text{ deg}$ . Pitch damping was calculated using both the steady-state lunar coning and transient planar pitching methods (36–38).

The Magnus moment for the body-alone configuration was very nonlinear, ranging from -0.77 at  $\alpha = 1$  deg to +0.10 at  $\alpha = 12$  deg. The Magnus moment for the 11120 configuration was positive and nearly constant, with values ranging from 0.25 to 0.5. The pitch-damping moment was more difficult to accurately predict than other projectiles previously analyzed. The combination of nearly incompressible flow and very small pitch-damping values (on the order of 1) due to the low length-to-diameter (L/D) ratio is the likely reason. It was difficult to obtain linear results using the lunar coning method—an inherent assumption of this method. For the planar pitching, the results were converged to a lower tolerance at each time step than past projectile geometries investigated at higher subsonic and supersonic Mach numbers. These issues are discussed in more depth in reference 31. The pitch-damping moments determined from the transient planar pitching method was more accurate than those from the steady-state lunar coning method. The pitch-damping values provided as input to the aerodynamic model were -1.24 for the body-alone configuration and -3.04 for the 11120 configuration.

All aerodynamic techniques (SEAP, WT, CFD) were utilized to provide the aerodynamic coefficient database. Subject matter expertise was applied to reconcile the best aerodynamic data available from various sources. The projectile body axial force coefficient, showing the WT, CFD, and merged (final database) data is shown in figure 18. Zero-yaw axial force is similar between WT and CFD methods and the yaw-dependent axial force is slightly higher for the CFD. Figure 19 provides the normal force of the control. The shape of the curves is similar for both the WT and CFD data. The CFD predicts about a 0.05 higher trim force coefficient. A summary of the aerodynamic database is given in tables 5–7. SEAP, WT, and CFD data are compiled along with the final merged dataset. Static aerodynamics, roll damping moment coefficient, and pitch damping moment coefficient for the projectile are in table 5. The nonlinear Magnus force and moment of the projectile are tabulated in table 6. Table 7 provides the aerodynamic coefficients for the control as a function of the stowed roll angle.

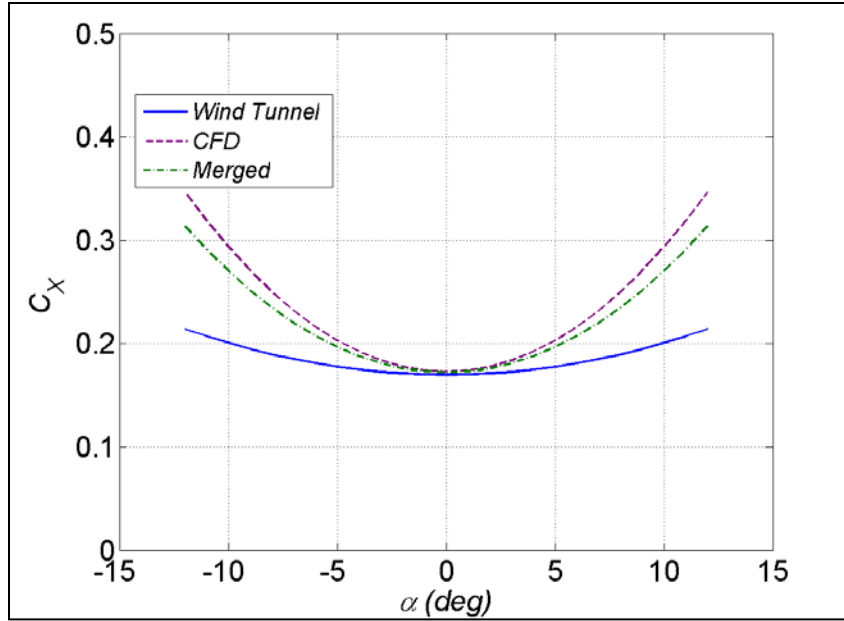


Figure 18. Axial force coefficient for projectile body.

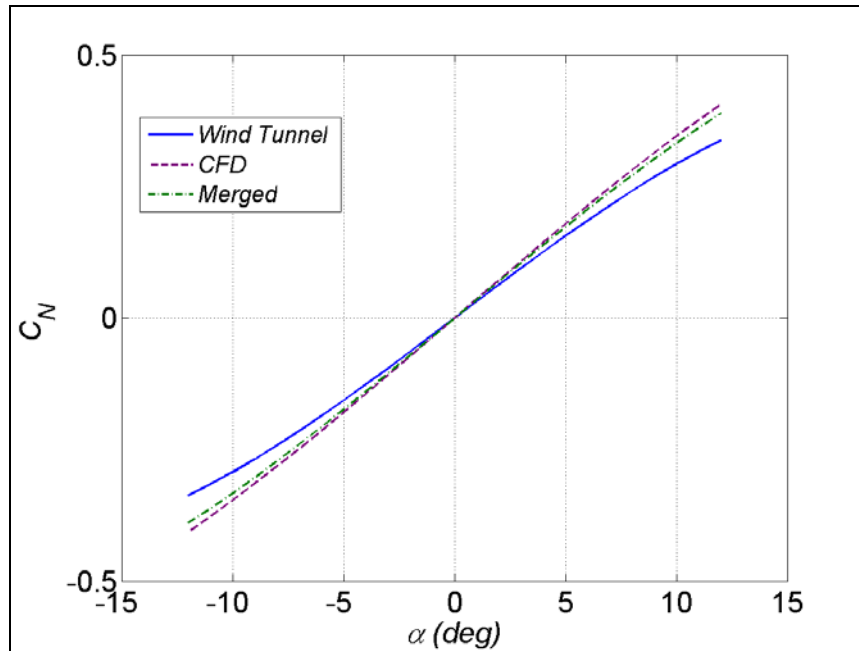


Figure 19. Normal force coefficient for control.

Table 5. Projectile aerodynamics.

Method	$C_{x_0}$	$C_{x_{\alpha^2}}$	$C_{N_{\alpha}}$	$C_{N_{\alpha^3}}$	$C_{m_{\alpha}}$	$C_{m_{\alpha^3}}$	$C_{l_p}$	$C_{m_q}$
SEAP	0.19820	2.1	2.08342	0	2.09488	0	-0.03055	-3.3
WT	0.169782	1.011851	1.829601	-4.94869	1.932517	-1.99989	NA	NA
CFD	0.172793	3.958777	2.076615	-3.07324	2.065624	0.423832	-0.02835	-1.24
Merged	0.17204	3.22205	2.01486	-3.54210	1.99907	-0.78803	-0.02937	-1.75500

Table 6. Projectile magnus aerodynamics.

Method	$\bar{\alpha}$ (deg)	0	1	2	3	4	5	7.5	10	15	20	30
SEAP	$C_{Y_{p\alpha}}$	-0.52	-0.52	-0.52	-0.52	-0.52	-0.52	-0.52	-0.52	-0.52	-0.52	-0.52
	$C_{n_{p\alpha}}$	-1.6	-1.54	-1.37	-1.13	-0.88	-0.7	0.05	0.03	0.03	0.02	0.01
CFD	$C_{Y_{p\alpha}}$	NA	0.392990 225	0.162194 013	NA	NA	- 0.374164 713	- 0.636513 499 <sup>a</sup>	NA	- 0.860910 632 <sup>a</sup>	NA	NA
	$C_{n_{p\alpha}}$	NA	- 0.598981 682	- 0.453168 691	NA	NA	- 0.124272 894	0.014947 658 <sup>a</sup>	NA	0.095972 186 <sup>b</sup>	NA	NA
Merged	$C_{Y_{p\alpha}}$	0.33784	0.16474	-0.00835	-0.14244	-0.27653	-0.41062	-0.57459	-0.69153	-0.77568	-0.77568	-0.77568
	$C_{n_{p\alpha}}$	-0.95860	-0.83424	-0.68238	-0.54015	-0.39543	-0.26820	0.00631	0.04909	0.07948	0.07698	0.07448

<sup>a</sup>CFD data collected at  $\bar{\alpha} = 8$  deg.

<sup>b</sup>CFD data collected and  $\bar{\alpha} = 12$  deg.

21

Table 7. Control aerodynamics for all stowed roll angles.

Method	$\hat{\phi}$ ,	$C_{X_0}$	$C_{X_\alpha}$	$C_{X_{\alpha^2}}$	$C_{X_{\alpha^3}}$	$C_{N_0}$	$C_{N_\alpha}$	$C_{N_{\alpha^3}}$	$C_{m_0}$	$C_{m_\alpha}$	$C_{m_{\alpha^3}}$
WT	0 deg	0.10598	0.48966	0.60734	0.08227	0.20748	0.46091	-1.19402	-0.11250	-0.20850	-0.20850
	30 deg	0.08936	0.48966	0.08423	0.08227	0.18315	0.45047	1.00463	-0.12169	-0.44139	0.49181
	60 deg	0.04008	0.48966	-0.16194	0.08227	0.09635	0.45974	4.04593	-0.08091	-0.39343	0.23514
	90 deg	0.03674	0.48966	-0.41301	0.08227	0.06707	0.31557	8.50209	-0.06287	-0.57775	0.75245
CFD	0 deg	0.11796	0.65287	0.78644	0.10969	0.21929	0.46867	-1.33984	-0.13927	-0.30858	-2.12313
Merged	0 deg	0.10598	0.48966	0.60734	0.08227	0.20748	0.46091	-1.19402	-0.11250	-0.20850	-0.20850
	30 deg	0.08936	0.48966	0.08423	0.08227	0.18315	0.45047	1.00463	-0.12169	-0.44139	0.49181
	60 deg	0.04008	0.48966	-0.16194	0.08227	0.09635	0.45974	4.04593	-0.08091	-0.39343	0.23514
	90 deg	0.03674	0.48966	-0.41301	0.08227	0.06707	0.31557	8.50209	-0.06287	-0.57775	0.75245

---

## 4. Aerodynamic Model

---

The aerodynamic model relates the aerodynamic coefficient data collected in experiments and computations to the aerodynamic forces and moments acting on a projectile in flight. Total aerodynamic forces and moments are separated into rigid and moveable surfaces.

$$\begin{aligned} X &= X^R + X^M \\ Y &= Y^R + Y^M \\ Z &= Z^R + Z^M \end{aligned} \quad (2)$$

$$\begin{aligned} L &= L^R + L^M \\ M &= M^R + M^M \\ N &= N^R + N^M \end{aligned} \quad (3)$$

Rigid aerodynamic surface forces include static (linear and nonlinear) and dynamic terms for the projectile body. Symbols in parenthesis indicate functional dependence of aerodynamic coefficients. The dynamic pressure is  $q = \frac{1}{2}\rho V^2$  and aerodynamic reference area is  $S = \frac{\pi}{4}D^2$  where  $D$  is the projectile diameter and  $V$  is the total velocity.

$$\begin{aligned} X^R &= -qS \left[ C_{X_0}(M) + C_{X_{\alpha^2}}(M)\alpha^2 \right] \\ Y^R &= -qS \left[ C_{N_\alpha}(M)\beta + C_{N_{\alpha^3}}(M)\beta^3 - C_{Y_{p\alpha}}(M, \bar{\alpha})\alpha \frac{pD}{2V} \right] \\ Z^R &= -qS \left[ C_{N_\alpha}(M)\alpha + C_{N_{\alpha^3}}(M)\alpha^3 + C_{Y_{p\alpha}}(M, \bar{\alpha})\beta \frac{pD}{2V} \right] \end{aligned} \quad (4)$$

Rigid aerodynamic surface moments include static (linear and nonlinear) and dynamic terms.

$$\begin{aligned} L^R &= qSD \left[ C_{l_p}(M) \frac{pD}{2V} \right] \\ M^R &= qS \left[ C_{m_\alpha}(M)\alpha + C_{m_{\alpha^3}}(M)\alpha^3 + C_{m_q}(M) \frac{qD}{2V} + C_{n_{p\alpha}}(M, \bar{\alpha})\beta \frac{pD}{2V} \right] \\ N^R &= qS \left[ -C_{m_\alpha}(M)\beta - C_{m_{\alpha^3}}(M)\beta^3 + C_{m_q}(M) \frac{rD}{2V} + C_{n_{p\alpha}}(M, \bar{\alpha})\alpha \frac{pD}{2V} \right] \end{aligned} \quad (5)$$

The following algorithm may be used to calculate moveable aerodynamic surface forces and moments for the  $i^{th}$  control mechanism. First, relevant roll angles for this problem are defined. Neglecting greater than 6 degrees-of-freedom (DOF) dynamics, the relative roll angle of the control mechanism is  $\Phi_i = -\phi + \phi_{CMD}$  (where  $\phi_{CMD}$  is the commanded roll direction of maneuver) and the Earth-fixed roll angle of the control mechanism is  $\phi_C = \phi + \Phi_i$ . The stowed roll angle of the  $i^{th}$  control mechanism then becomes  $\hat{\phi}_i = \Phi_i - \phi_{B_i}$  (where  $\phi_{B_i}$  is the roll angle of the control mechanism mounted in the projectile body).

Compute local velocity at each moveable aerodynamic surface from center-of-pressure (CP) data ( $x_{CP}$  is axial CP and  $r_{CP}$  is radial CP), geometry ( $\phi_{B_i}$ ), and 6 DOF states.

$$\vec{V}_{M_i/I} = \vec{V}_{CG/I} + \vec{\omega}_{B/I} \times \vec{r}_{CG \rightarrow CP_i} \quad (6)$$

where  $\vec{V}_{CG/I} = [u \ v \ w]^T$ ,  $\vec{\omega}_{B/I} = [p \ q \ r]^T$ , and  $\vec{r}_{CG \rightarrow CP_i} = [x_{CP} \ r_{CP} \cos(\phi_{B_i}) \ r_{CP} \sin(\phi_{B_i})]^T$ .

Obtain velocity in  $i^{th}$  moveable aerodynamic surface coordinates ( $[u_{M_i} \ v_{M_i} \ w_{M_i}]^T$ ) using the transformation matrix.

$$\vec{T}_{BM_i} = \begin{bmatrix} 1 & 0 & 0 \\ 0 & \cos(\Phi_i) & \sin(\Phi_i) \\ 0 & -\sin(\Phi_i) & \cos(\Phi_i) \end{bmatrix} \quad (7)$$

Calculate total and local moveable aerodynamic surface angle-of-attack.

$$\begin{aligned} \bar{\alpha}_{M_i} &= a \sin \left( \frac{\sqrt{v_{M_i}^2 + w_{M_i}^2}}{\sqrt{u_{M_i}^2 + v_{M_i}^2 + w_{M_i}^2}} \right) \\ \beta_{M_i} &= a \sin \left( \frac{v_{M_i}}{\sqrt{u_{M_i}^2 + v_{M_i}^2 + w_{M_i}^2}} \right) \end{aligned} \quad (8)$$

Determine moveable aerodynamic surface axial force, normal force, roll moment, and pitching moment coefficients. Side forces and side moments on the moveable aerodynamic surface are neglected.

$$\begin{aligned} C_X^{M_i} &= C_{X_0}^M(M, \hat{\phi}_i) + C_{X_{\alpha_M}}^M(M, \hat{\phi}_i)\beta_{M_i} + C_{X_{\alpha^2_M}}^M(M, \hat{\phi}_i)\beta_{M_i}^2 + C_{X_{\alpha^3_M}}^M(M, \hat{\phi}_i)\beta_{M_i}^3 \\ C_Z^{M_i} &= C_{Z_0}^M(M, \hat{\phi}_i) + C_{Z_{\alpha_M}}^M(M, \hat{\phi}_i)\beta_{M_i} + C_{Z_{\alpha^3_M}}^M(M, \hat{\phi}_i)\beta_{M_i}^3 \\ C_l^{M_i} &= C_{l_0}^M(M, \hat{\phi}_i) + C_{l_{\alpha_M}}^M(M, \hat{\phi}_i)\bar{\alpha}_{M_i} \\ C_m^{M_i} &= C_{m_0}^M(M, \hat{\phi}_i) + C_{m_{\alpha_M}}^M(M, \hat{\phi}_i)\beta_{M_i} + C_{m_{\alpha^3_M}}^M(M, \hat{\phi}_i)\beta_{M_i}^3 \end{aligned} \quad (9)$$

Compute moveable aerodynamic surface axial force, normal force, roll moment, and pitching moment.

$$\begin{aligned} X^{M_i} &= -q_{M_i} S C_X^{M_i} \\ Y^{M_i} &= -q_{M_i} S C_Z^{M_i} \\ L^{M_i} &= -q_{M_i} S D C_l^{M_i} \\ N^{M_i} &= -q_{M_i} S D C_m^{M_i} \end{aligned} \quad (10)$$

Transform moveable aerodynamic surface forces and moments to body coordinates.

$$\begin{aligned} \begin{bmatrix} X^{M_i} \\ Y^{M_i} \\ Z^{M_i} \end{bmatrix}_B &= \vec{T}_{BM_i}^{-1} \begin{bmatrix} X^{M_i} \\ Y^{M_i} \\ 0 \end{bmatrix}_{M_i} \\ \begin{bmatrix} X^{M_i} \\ Y^{M_i} \\ Z^{M_i} \end{bmatrix}_B &= \vec{T}_{BM_i}^{-1} \begin{bmatrix} L^{M_i} \\ 0 \\ N^{M_i} \end{bmatrix}_{M_i} \end{aligned} \quad (11)$$

## 5. Flight Mechanics

The equations of motion are formulated in the inertial frame while the body frame was used for collection of aerodynamic data. In this report, the Earth coordinate system (subscript E) is used for the inertial frame and the body-fixed coordinate system (subscript B) is used for the body frame. These right-hand coordinate systems are related by the Euler angles for roll ( $\phi$ ), pitch ( $\theta$ ), and yaw ( $\psi$ ) as shown in figure 20.

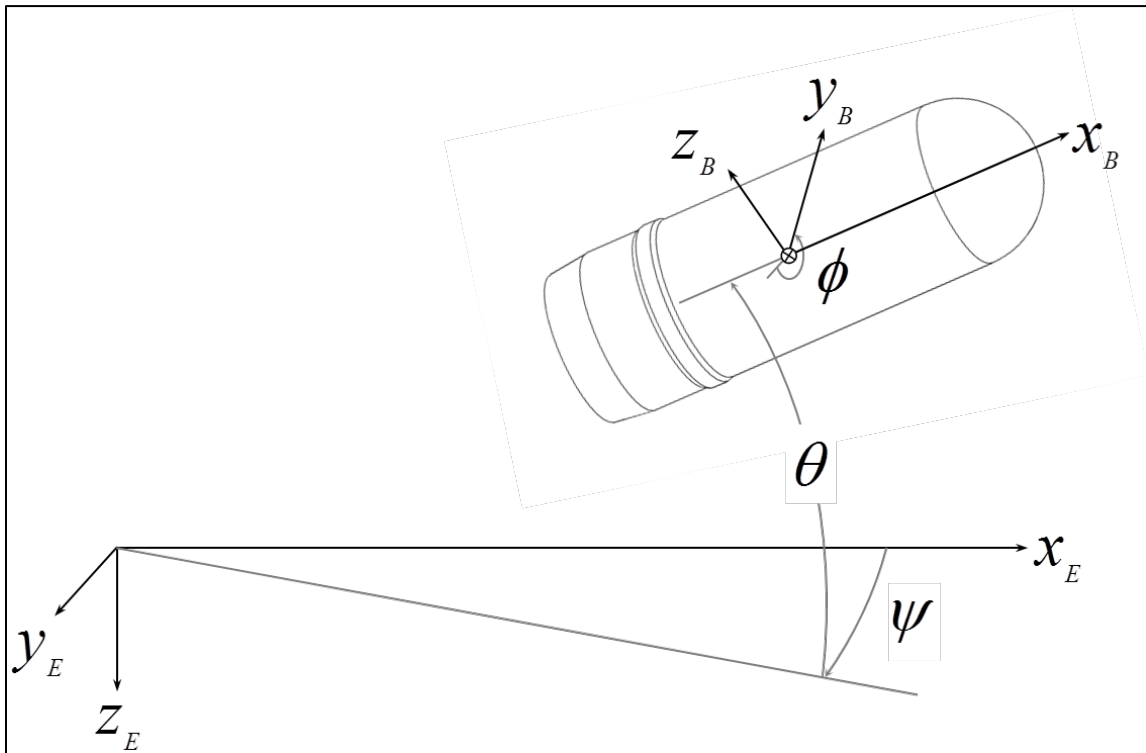


Figure 20. Earth and body-fixed coordinate systems and Euler angles.

Rotating through the sequence of Euler angles yields the transformation matrix from quantities in body-fixed coordinates to Earth coordinates.

$$\vec{T}_{BE} = \begin{bmatrix} c_\theta c_\psi & s_\phi s_\theta c_\psi - c_\phi s_\psi & c_\phi s_\theta c_\psi + s_\phi s_\psi \\ c_\theta s_\psi & s_\phi s_\theta s_\psi + c_\phi c_\psi & c_\phi s_\theta s_\psi + s_\phi c_\psi \\ -s_\theta & s_\phi c_\theta & c_\phi c_\theta \end{bmatrix} \quad (12)$$

Projectile flight states are center-of-gravity position  $[x \ y \ z]^T$ , attitude  $[\phi \ \theta \ \psi]^T$ , body translational velocity  $[u \ v \ w]^T$ , and body rotational velocity  $[p \ q \ r]^T$ . Translational and rotational kinematics for the body-fixed coordinate system are provided below (1, 2).

$$\begin{bmatrix} \dot{x} \\ \dot{y} \\ \dot{z} \end{bmatrix} = \begin{bmatrix} c_\theta c_\psi & s_\phi s_\theta c_\psi - c_\phi s_\psi & c_\phi s_\theta c_\psi + s_\phi s_\psi \\ c_\theta s_\psi & s_\phi s_\theta s_\psi + c_\phi c_\psi & c_\phi s_\theta s_\psi + s_\phi c_\psi \\ -s_\theta & s_\phi c_\theta & c_\phi c_\theta \end{bmatrix} \begin{bmatrix} u \\ v \\ w \end{bmatrix} \quad (13)$$

$$\begin{bmatrix} \dot{\phi} \\ \dot{\theta} \\ \dot{\psi} \end{bmatrix} = \begin{bmatrix} 1 & s_\phi t_\theta & c_\phi t_\theta \\ 0 & c_\phi & -s_\phi \\ 0 & s_\phi/c_\theta & c_\phi/c_\theta \end{bmatrix} \begin{bmatrix} p \\ q \\ r \end{bmatrix} \quad (14)$$

Newtonian kinetics may be applied to a projectile in free-flight. The translational and rotational dynamics are expressed in body-fixed coordinates (1, 2).

$$\begin{bmatrix} \dot{u} \\ \dot{v} \\ \dot{w} \end{bmatrix} = \frac{1}{m} \begin{bmatrix} X + X_G \\ Y + Y_G \\ Z + Z_G \end{bmatrix} - \begin{bmatrix} 0 & -r & q \\ r & 0 & -p \\ -q & p & 0 \end{bmatrix} \begin{bmatrix} u \\ v \\ w \end{bmatrix} \quad (15)$$

$$\begin{bmatrix} \dot{p} \\ \dot{q} \\ \dot{r} \end{bmatrix} = \vec{I}^{-1} \begin{bmatrix} L \\ M \\ N \end{bmatrix} - \vec{I}^{-1} \begin{bmatrix} 0 & -r & q \\ r & 0 & -p \\ -q & p & 0 \end{bmatrix} \vec{I} \begin{bmatrix} p \\ q \\ r \end{bmatrix} \quad (16)$$

The forcing functions in the governing equations have components due to aerodynamics and gravity. The aerodynamic model is provided earlier. Gravity acts only as a force ( $[X_G \ Y_G \ Z_G]^T = \vec{T}_{BE}^T [0 \ 0 \ g]^T$ ).

## 6. Delivery in the Ballistic Environment

The process of delivering a lethal payload via a man portable weapon in the ballistic environment must be described and modeled. First, the target location (and sometimes gun location) is measured or estimated. For direct fire engagements (line of sight), these data are obtained from a rangefinder device or a human guess. Targeting information comes through a

network from a collective asset for indirect fire (or more complex direct fire) engagements. Regardless of the targeting method, there is uncertainty associated with the data.

A fire control solution, or desired weapon pointing angle, is determined based on the targeting data. The weapon is aimed, sometimes through the use of an iron sight or an aim-assist device, and the projectile launched. Errors are associated with these processes because the fire control solution is never perfect, the weapon cannot precisely achieve the desired aiming angles, and the launch has variability in the muzzle velocity and angular rates of the projectile.

The projectile flies through the atmosphere on the way to the target. Atmospheric density, sound speed, and wind vary throughout time and space and influence projectile flight. Another factor that affects the projectile flight is physical variability. The mass properties and aerodynamics change from round to round due to effects such as manufacturing tolerances.

The fuze prescribes the terminating location of the projectile. A variety of fuzing mechanisms, point-detonating, proximity, time, or turns-count, are available. The method and uncertainty dictate the burst point of the warhead.

Table 8 provides the models and input data used in this paper for these delivery processes. Uniform (U) and normal (N) distributions are used throughout the modeling. The targeting module assumes a rangefinder device estimates the range-to-target ( $R_T$ ) which in turn corrupts the fire control solution. Aiming assumes a supported weapon. Spin-stabilized projectile drift is accounted for in the azimuth ( $1, 2$ ). Muzzle velocity is modeled based on recoil impulse limitations and propulsion efficiency. The spin rate at launch is prescribed by the muzzle velocity and gun twist to within variation of the rifling engagement. Atmospheric density is perturbed from the 1962 International Standard Atmosphere (ISA). Wind is modeled as a constant horizontal component over the flight in any direction. All fuzes burst at a nominal point for that fire control solution (e.g., range-to-go [ $R_{go}$ ] for proximity, time to range [ $t_f$ ] for time, roll angle to range [ $\phi_f$ ] for turns) to within some tolerance due to relevant effects such as radio-frequency ranging, clock errors, or turn quantization.

Table 8. Models and data for man portable delivery process.

Category	Process	Model	Data
Targeting	Targeting	$R_T = \mathbb{U}(\hat{R}_T, \pm\sigma_R)$	$\sigma_R = 3 \text{ m}$
Launch	Weapon elevation	$\theta_0 = \mathbb{N}(f(R_T), \sigma_\theta)$	table $\hat{\theta}_0 = f(R_T)$ , $\sigma_\theta = 0.0014 \text{ rad.}$
	Weapon azimuth	$\psi_0 = \mathbb{N}(f(R_T, \theta_0), \sigma_\psi)$	table $\hat{\psi}_0 = f(R_T, \theta_0)$ , $\sigma_\psi = 0.0014 \text{ rad.}$
	Velocity	$V_0 = \mathbb{N}(\frac{I_R}{f_p m}, \sigma_V)$	$I_R = 24.5 \text{ N-s}$ , $f_p = 1.1$ , $\sigma_V = 2 \text{ m/s}$
	Spin rate	$p_0 = \mathbb{N}(V_0 \frac{2\pi}{\Omega D}, V_0 \frac{2\pi}{\Omega D} \sigma_p)$	$\Omega = 30 \text{ calibers/rev}$ , $\sigma_p = 0.0035 \%$
	Pitch rate	$q_0 = \mathbb{N}(0, \sigma_q)$	$\sigma_q = 2 \text{ rad/s}$
	Yaw rate	$r_0 = \mathbb{N}(0, \sigma_r)$	$\sigma_r = 2 \text{ rad/s}$
Atmosphere	Density	$\rho(z) = \mathbb{N}(1962 \text{ ISA}, \sigma_\rho)$	$\sigma_\rho = 0.015\%$
	Wind speed	$V_w = \mathbb{N}(0, \sigma_{V_w})$	$\sigma_{V_w} = 3.36 \text{ m/s}$
	Wind direction	$\theta_w = \mathbb{U}(0, \sigma_{\theta_w})$	$\sigma_{\theta_w} = 2\pi \text{ rad}$
Mass Properties	Mass	$m = \mathbb{N}(\hat{m}, \sigma_m)$	$\hat{m} = 0.342 \text{ kg}$ , $\sigma_m = 0.5 \%$
	Diameter	$D = \mathbb{N}(\hat{D}, \sigma_D)$	$\hat{D} = 0.040 \text{ m}$ , $\sigma_D = 0.1 \%$
	Axial inertia	$I_X = \mathbb{N}(\hat{I}_X, \sigma_{I_X})$	$\hat{I}_X = 8.54\text{e-}5 \text{ kg-m}^2$ , $\sigma_{I_X} = 3 \%$
	Transverse inertia	$I_T = \mathbb{N}(\hat{I}_T, \sigma_{I_T})$	$\hat{I}_T = 3.56\text{e-}4 \text{ kg-m}^2$ , $\sigma_{I_T} = 1 \%$
Aerodynamics	Axial force	$C_X = \mathbb{N}(\hat{C}_X, \sigma_{C_X})$	$\hat{C}_X$ (see aero tables), $\sigma_{C_X} = 2 \%$
	Normal force	$C_N = \mathbb{N}(\hat{C}_N, \sigma_{C_N})$	$\hat{C}_N$ (see aero tables), $\sigma_{C_N} = 5 \%$
	Pitching moment	$C_m = \mathbb{N}(\hat{C}_m, \sigma_{C_m})$	$\hat{C}_m$ (see aero tables), $\sigma_{C_m} = 4 \%$
	Roll damping Moment	$C_{I_p} = \mathbb{N}(\hat{C}_{I_p}, \sigma_{C_{I_p}})$	$\hat{C}_{I_p}$ (see aero tables), $\sigma_{C_{I_p}} = 5 \%$
	Pitch damping moment	$C_{m_q} = \mathbb{N}(\hat{C}_{m_q}, \sigma_{C_{m_q}})$	$\hat{C}_{m_q}$ (see aero tables), $\sigma_{C_{m_q}} = 15 \%$
	Magnus force	$C_{Y_{p\alpha}} = \mathbb{N}(\hat{C}_{Y_{p\alpha}}, \sigma_{C_{Y_{p\alpha}}})$	$\hat{C}_{Y_{p\alpha}}$ (see aero tables), $\sigma_{C_{Y_{p\alpha}}} = 15 \%$
	Magnus moment	$C_{n_{p\alpha}} = \mathbb{N}(\hat{C}_{n_{p\alpha}}, \sigma_{C_{n_{p\alpha}}})$	$\hat{C}_{n_{p\alpha}}$ (see aero tables), $\sigma_{C_{n_{p\alpha}}} = 15 \%$
Fuzing	Proximity	$R_{go} = \mathbb{N}(\hat{R}_{go}, \sigma_{R_{go}})$	$\hat{R}_{go} = 3 \text{ m}$ , $\sigma_{R_{go}} = 0.5 \text{ m}$
	Time	$t_f = \mathbb{N}(f(R_T), \sigma_t)$	table $\hat{t}_f = f(R_T)$ , $\sigma_t = 0.05 \%$
	Turns-count	$\phi_f = \mathbb{U}(f(R_T), \pm\sigma_{\phi_f})$	table $\hat{\phi}_f = f(R_T)$ , $\sigma_{\phi_f} = \pi/2 \text{ rad}$

## 7. Delivery Characterization

The ballistic delivery accuracy was assessed. The models and input data previously described for the targeting, launch, atmosphere, mass properties, aerodynamics, and fuzing were implemented in a Monte Carlo simulation of the flight mechanics. The target was placed at 200 m. Burst points were compiled with point-detonating, proximity, time, and turns-count fuzes. Figures 21–22 show three-dimensional burst points for ballistic flight. All point-detonating fuze cases impact on the ground plane. Time and turns-count fuzes stand the bursts up more in the vertical plane. All

results feature significant spread in the downrange direction (usually more than 10 m) since the launch is relatively low elevation (approximately 15 deg). The crossrange dispersion was usually less than 1–2 m.

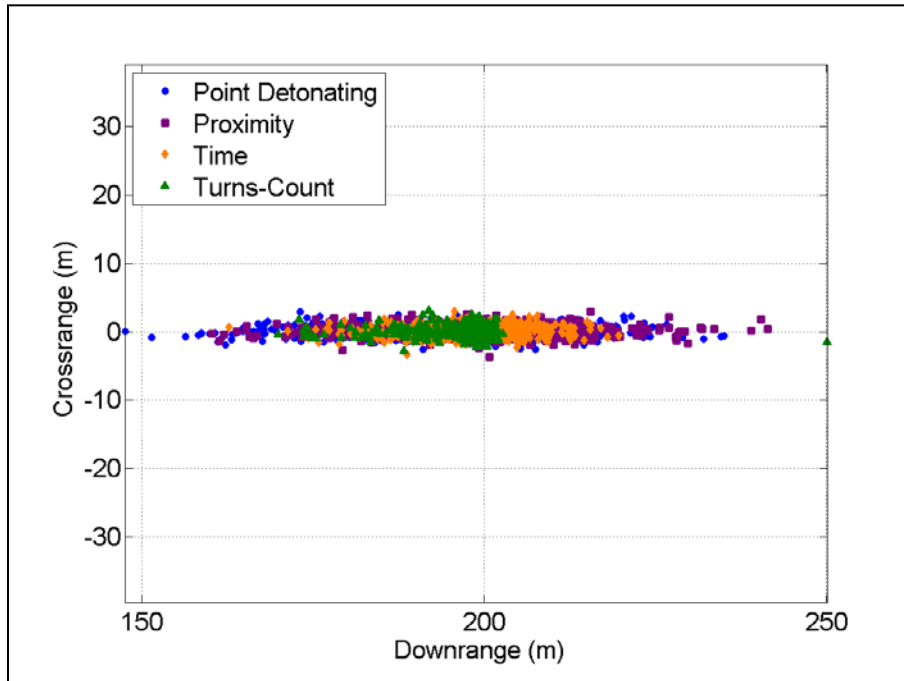


Figure 21. Horizontal plane ballistic burst points.

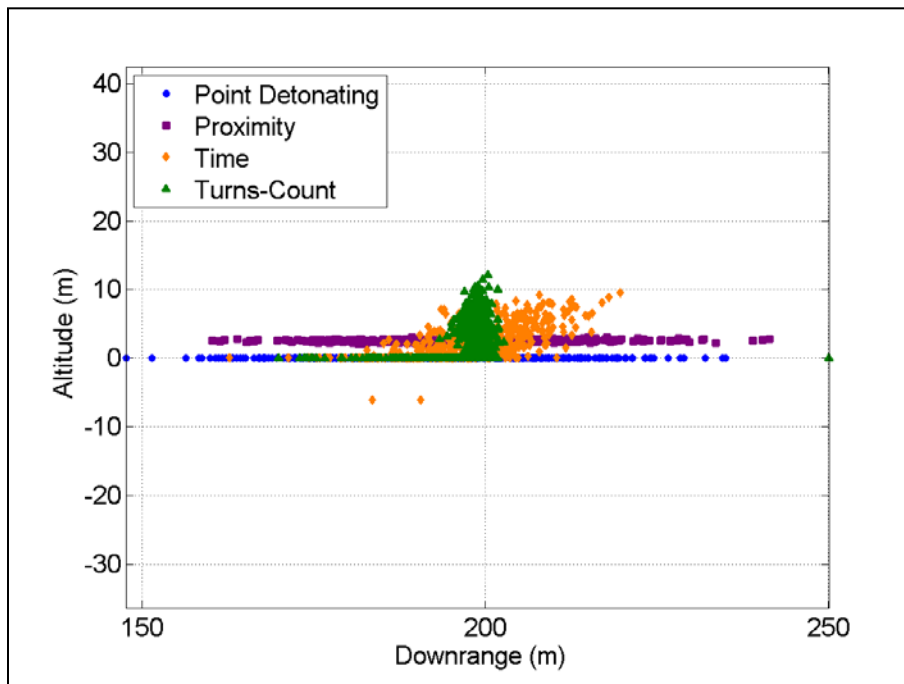


Figure 22. Vertical plane ballistic burst points.

Ballistic delivery accuracy provides a metric for initial assessment of the feasibility of this small diameter guided projectile concept. The control authority afforded by this concept must be larger than the ballistic dispersion. The aerodynamic data collected in the WT (contained in tables 3–4) was used to quantify the maneuver footprint of the various configurations. Flight simulations were conducted with nominal launch, atmosphere, mass properties, and aerodynamics with an elevation that reaches a ballistic range of 200 m. Maneuvers began at launch and continued throughout flight to ground impact. Maneuver direction was varied across eight, equally distributed angles to provide a sense of crossrange and downrange course corrections available.

Figure 23 demonstrates the control authority footprint for the different airfoil profiles with a two-actuator variant. In general, the projectile flies furthest downrange for a maneuver up since this represents the longest time-of-flight. The difference between the maneuver down and the ballistic impact point is larger than the differences for the maneuver left or right mainly due to the angle-of-fall (near 20 deg from horizontal). The greater normal force provided by the cambered airfoil yields significantly more control authority. Comparing the horizontal plane control authority for the NACA 4412 airfoil with the ballistic burst points suggests that maneuverability is sufficient to account for sources of delivery error.

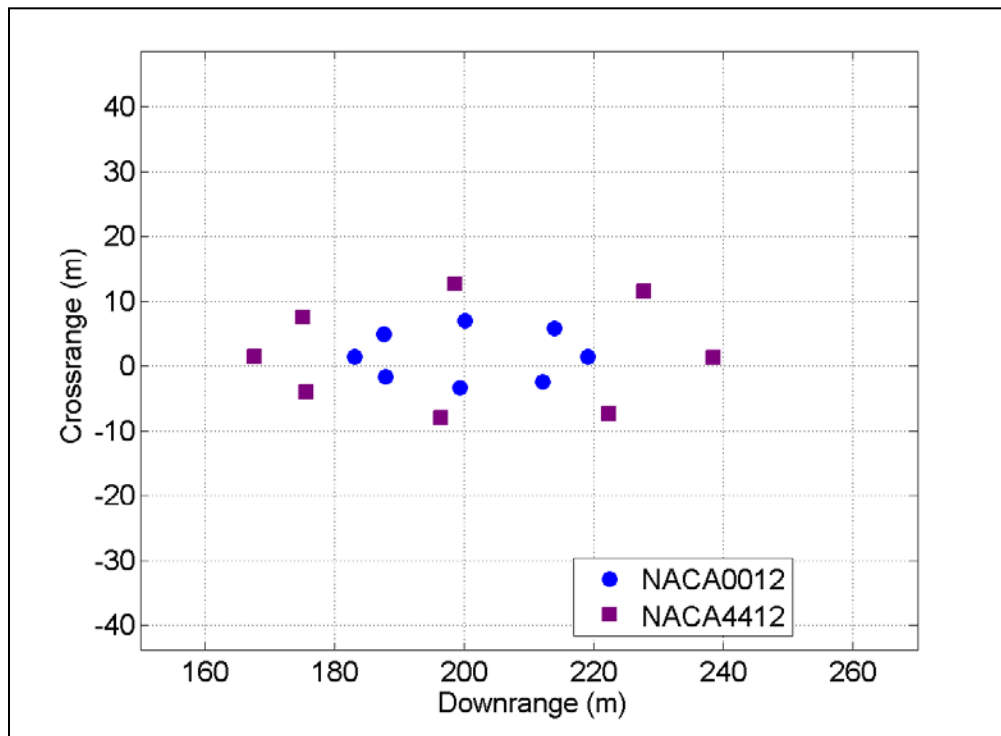


Figure 23. Ground plane control authority for airfoil parameter.

The total downrange and crossrange course corrections were calculated from the horizontal plane maneuver impacts for the airfoil parameter. These data, provided in figure 24, quantify an almost factor of 2 increase in the downrange and crossrange control authority for the cambered airfoil over the symmetric airfoil.

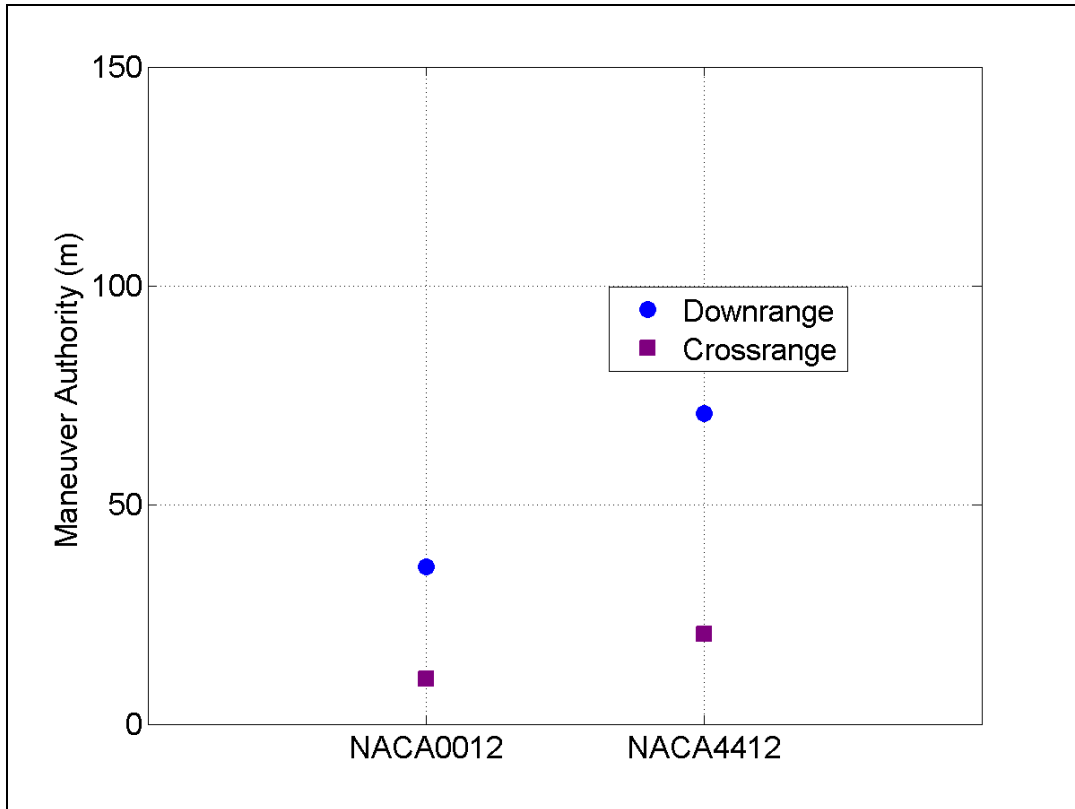


Figure 24. Control authority for airfoil parameter.

The downrange and crossrange maneuver authority was calculated for a wider parameter set in a manner similar to that shown for the airfoil parameter. Figure 25 illustrates that the larger planform of the wing increases the control authority. Examination of the results in figure 26 indicates that control authority increases nearly linearly with the wing deflection angle. The data for the standoff distance shown in figure 27 quantifies how getting the wing further away from the projectile increases maneuverability. Finally, adding more wings as provided in figure 28 linearly increases the control authority.

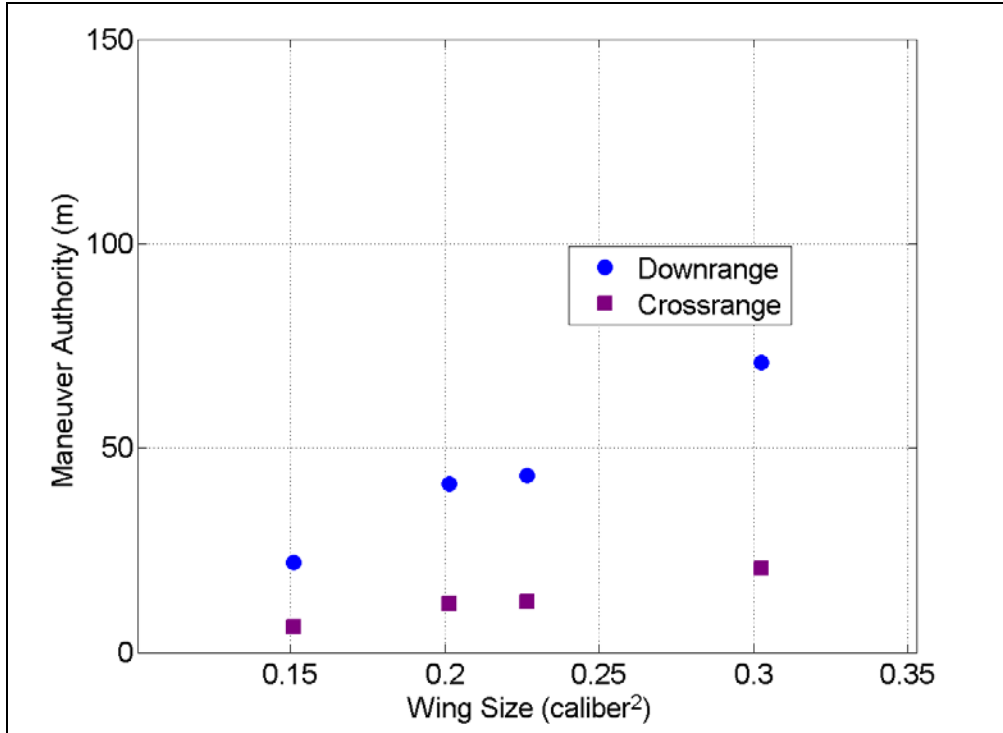


Figure 25. Control authority for planform parameter.

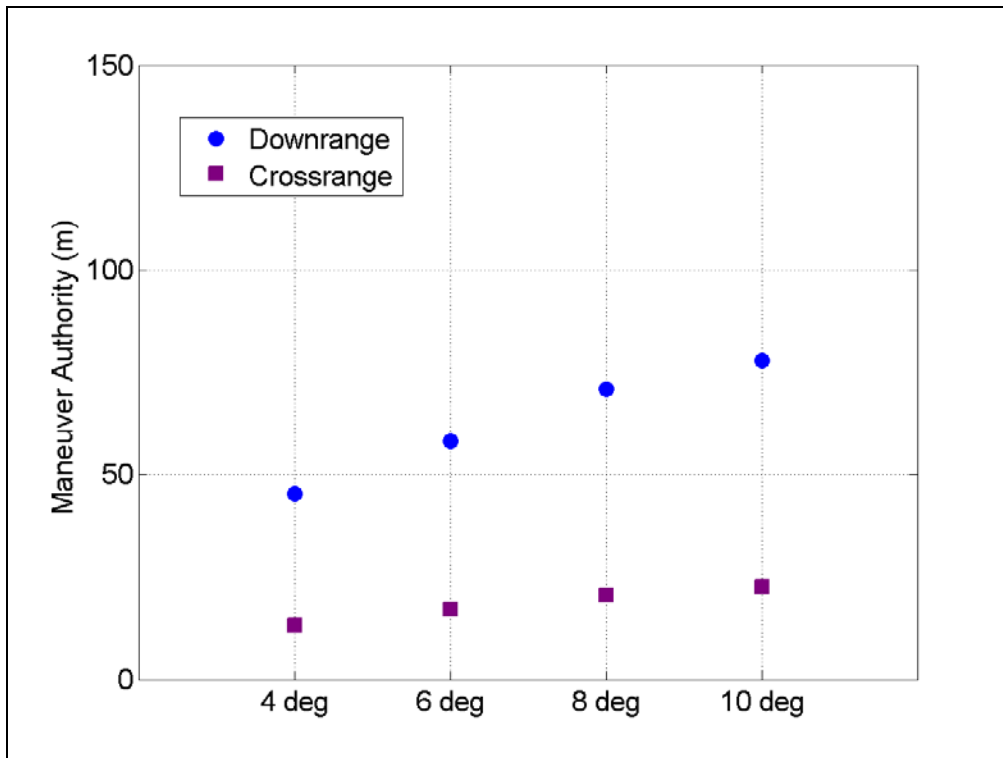


Figure 26. Control authority for deflection parameter.

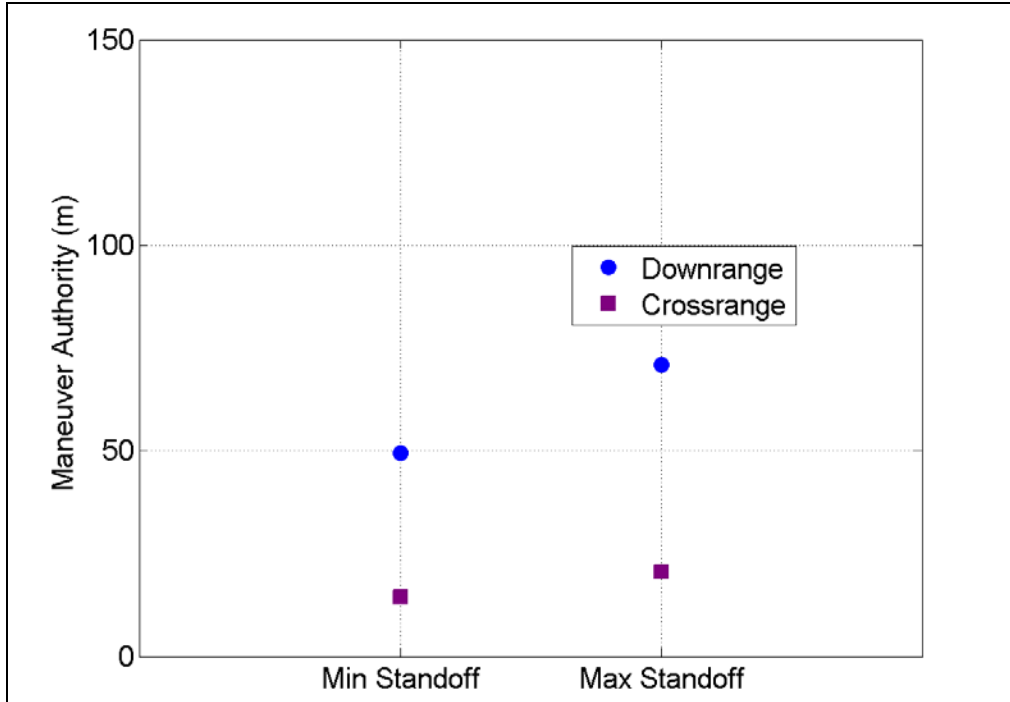


Figure 27. Control authority for standoff parameter.

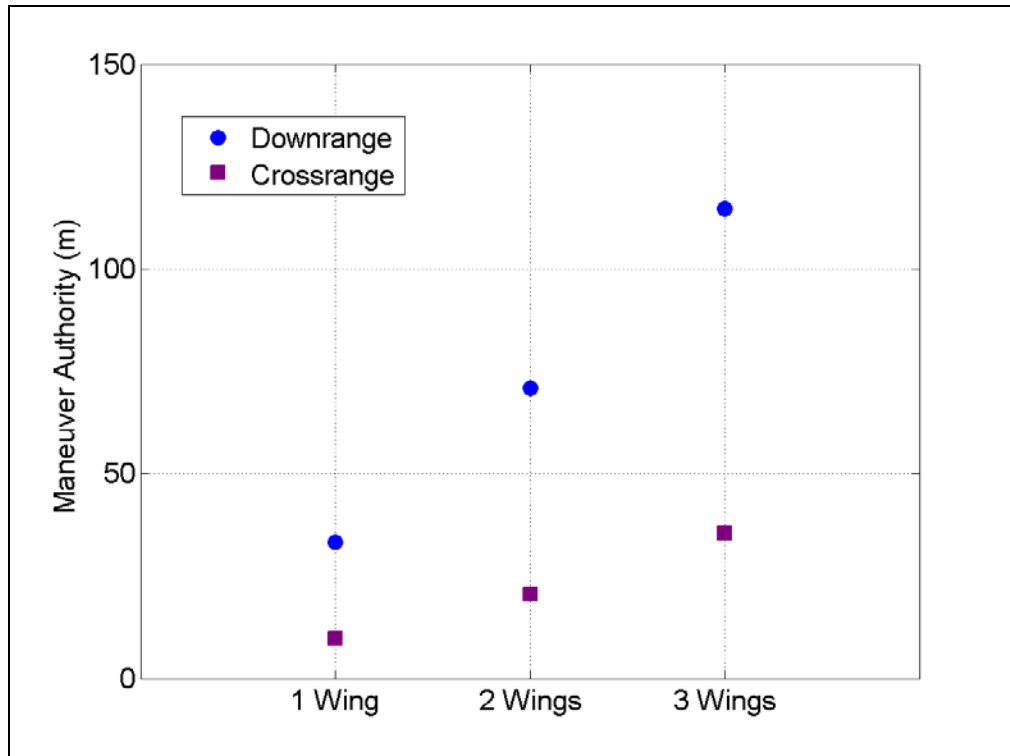


Figure 28. Control authority for number of wings.

Control authority was larger than the ballistic dispersion for a significant subset of the wing parameters. The results of the parametric study of maneuverability and practical packaging considerations suggest a best set of wing characteristics. These parameters included a two-actuator variant with a NACA 4412 airfoil sized to 0.48-cal. chord  $\times$  0.61-cal. span deflected to 8 deg with maximum standoff. The CFD aerodynamic predictions were performed with this configuration and the results presented in the remainder of this report possess the aerodynamic coefficients for this geometry (as given in tables 5–7).

Typical maneuver flight response is outlined in figures 29–33. The down-selected configuration was launched at approximately 15 deg under nominal conditions and an up maneuver was commanded throughout the flight. The pitch angle-of-attack history shows that the maneuver excites the precession and nutation modes. Precession is evident in the lower frequency, higher amplitude oscillation angular motion. The maneuver concept induces an angle-of-attack in the projectile just over 4 deg. The yaw angle-of-attack demonstrates similar precession and nutation motion. Yaw of repose over about 1 deg for this spin rate and launch elevation can be seen. This projectile features a launch spin rate of about 54 Hz (corresponding to a gyroscopic stability factor around 2.3) and decreases about 2 Hz over 4 s. Mach number decreases throughout flight from just under 0.2 at launch. The vertical plane trajectory demonstrates that the range is extended over 50 m past the ballistic impact point (200-m ballistic range at this elevation) from the maneuver concept inducing a 4-deg angle-of-attack. No deleterious flight instabilities were encountered during flight simulations.

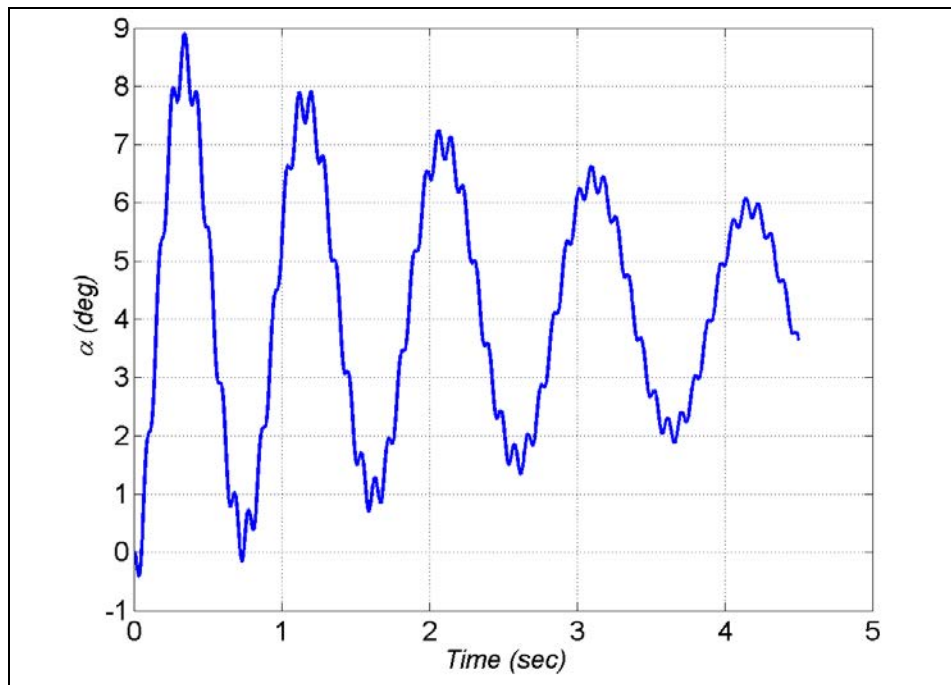


Figure 29. Pitch angle-of-attack for maneuver up.

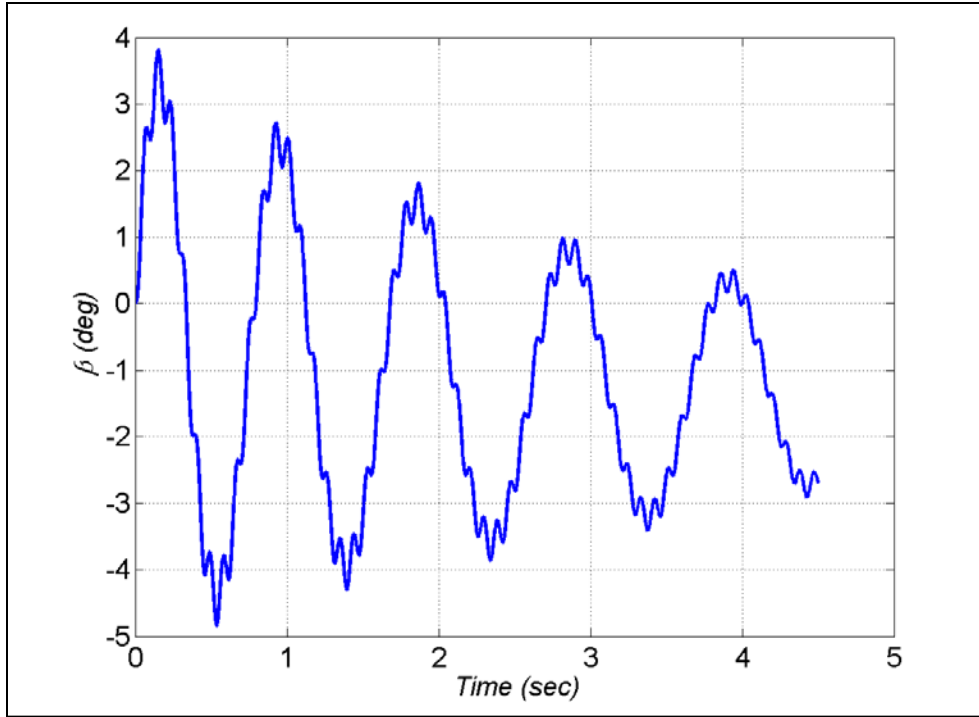


Figure 30. Yaw angle-of-attack for maneuver up.

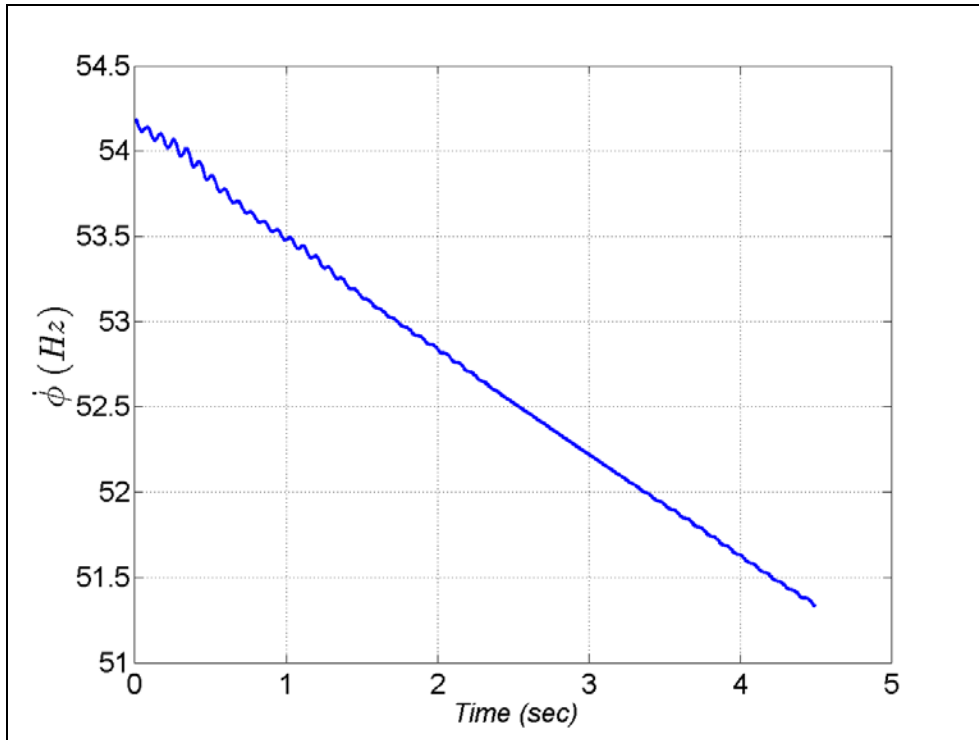


Figure 31. Spin rate for maneuver up.

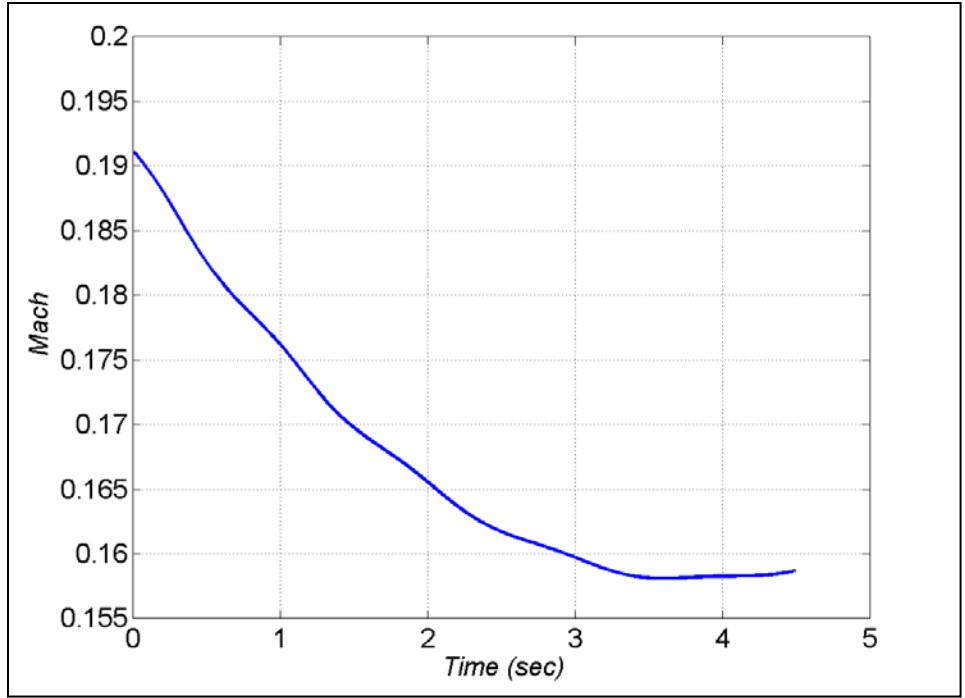


Figure 32. Mach number for maneuver up.

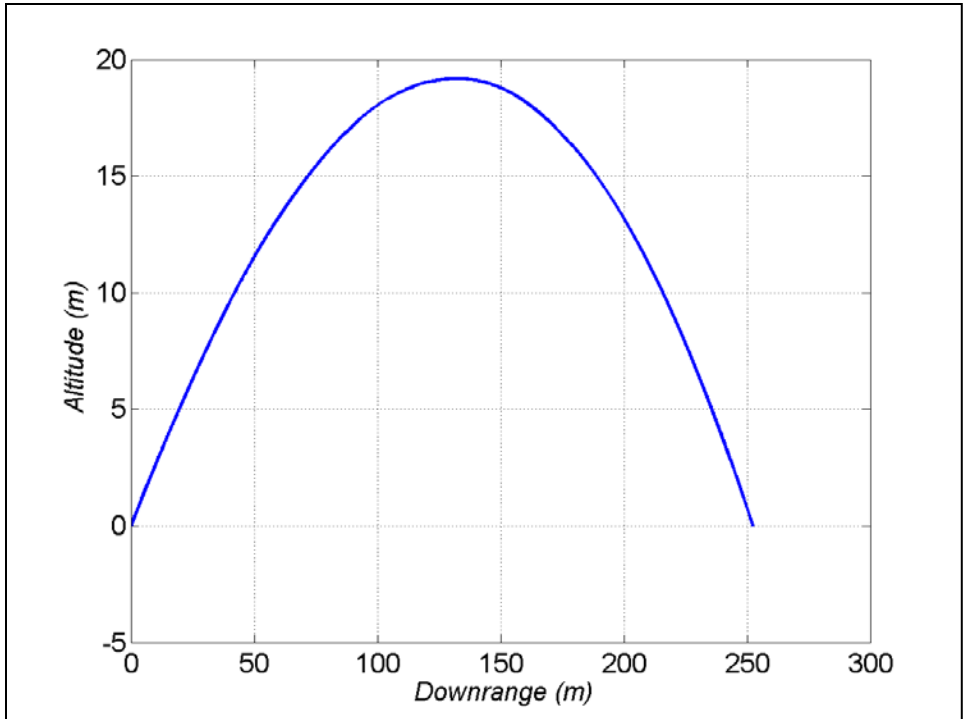


Figure 33. Vertical plane trajectory for maneuver up.

---

## 8. Conclusions

---

This study demonstrated the utility of a new concept for maneuvering a small-diameter projectile. The concept was detailed and the aerodynamics of this shape was determined using a variety of techniques. WT experiments were conducted on numerous wing geometries for initial feasibility. Experimental data were used to down-select the configuration and validate CFD predictions prior to applying the computations for more advanced purposes such as determining dynamic derivatives.

An aerodynamic model to relate WT- and CFD-derived coefficients to free-flight forces and moments was derived specifically for this novel configuration. Effects such as the time-dependent (or roll history) exposure of the wing to the airstream were included in the model.

The nonlinear mechanics underpinning flight simulations were presented. The delivery process and modeling of a lethal payload via this guided flight concept was summarized. Physics-based models and input data for targeting, and variation due to launch, atmosphere, physical characteristics, and fuzing were outlined. Delivery characterizations were performed via simulation to assess control authority requirements.

Realistic maneuver footprints were obtained through flight simulation. Trade studies were conducted to quantify the relationship between wing parameters and control authority. A characteristic set of flight dynamic metrics were provided for understanding guided flight behavior.

This study indicates that control authority of this novel concept is sufficient to compensate for ballistic delivery error sources. These results were obtained despite the challenges associated with flying a small-diameter, spin-stabilized projectile with low-dynamic pressure. The components involved with implementing this concept are low cost (e.g., commercial DC motors). These technologies support realization of a new class of precision weapons for the Army at the squad level.

Future computational and experimental efforts focus on understanding the effects of the transient wing exposure to the airstream on the flight behavior. Additionally, mechatronic design and evaluation (to include gun hardening) of the actuation technology must be performed.

---

## 9. References

---

1. Murphy, C. H. *Free Flight Motion of Symmetric Missiles*; U.S. Army Ballistic Research Laboratory: Aberdeen Proving Ground, MD, BRL-1216, July 1963.
2. McCoy, R. L. *Modern Exterior Ballistics*; Schiffer Publishing Ltd.: Atlen, PA, 1999.
3. Lloyd, K. H.; Brown, D. P. Instability of Spinning Projectiles During Terminal Guidance. *Journal of Guidance, Control, and Dynamics* **1979**, 2 (1), 65–70.
4. Murphy, C. H. Instability of Controlled Projectiles in Ascending or Descending Flight. *Journal of Guidance, Control, and Dynamics* **1981**, 4 (1), 66–69.
5. Regan, F. J.; Smith, J. Aeroballistics of a Terminally Corrected Spinning Projectile. *Journal of Spacecraft and Rockets* **1975**, 12, 733–738.
6. Moorhead, J. S. Precision Guidance Kits (PGKs): Improving the Accuracy of Conventional Cannon Rounds. *Field Artillery* January–February **2007**, 31–33.
7. Fresconi, F.; Cooper, G. R.; Celmins, I.; DeSpirito, J.; Costello, M. Flight Mechanics of a Novel Guided Spin-Stabilized Projectile Concept. *Journal of Aerospace Engineering* **2011**, 226, pp. 327–340.
8. Theodoulis, S.; Gassmann, V.; Wernert, P.; Dritsas, L.; Kitsios, I.; Tzes, A. Guidance and Control Design for a Class of Spin-Stabilized Fin-Controlled Projectiles. *Journal of Guidance, Control, and Dynamics* **2013**, 36, 517–531.
9. Gross, M.; Costello, M.; Fresconi, F. Impact Point Model Predictive Control of a Spin-Stabilized Projectile with Instability Protection. *Atmospheric Flight Mechanics Conference Proceedings*, AIAA-2013, 2013.
10. Ollerenshaw, D.; Costello, M. Simplified Projectile Swerve Solution for General Control Inputs. *Journal of Guidance, Control, and Dynamics* **2008**, 3 (1), 1259–1265.
11. Fresconi, F.; Plostins, P. Control Mechanism Strategies for Spin-Stabilized Projectiles. *Journal of Aerospace Engineering* **2010**, 224, 979–991.
12. Cooper, G.; Costello, M. Flight Dynamic Response of Spinning Projectiles to Lateral Impulsive Loads. *Journal of Dynamic Systems, Measurement, and Control* **2004**, 126, 605–613.
13. Davis, B.; Malejko, G.; Dorhn, R.; Owens, S.; Harkins, T.; Bischer, G. Addressing the Challenges of a Thruster-Based Precision Guided Mortar Munition With the Use of Embedded Telemetry Instrumentation. *ITEA Journal* **2009**, 30, 117–125.

14. Sahu, J.; Fresconi, F.; Heavey, K. Unsteady Aerodynamic Simulations of a Finned Projectile at a Supersonic Speed with Jet Interaction. *Atmospheric Flight Mechanics Conference Proceedings*, AIAA-2013, 2014.
15. Brandeis, J.; Gill, J. Experimental Investigation of Super- and Hypersonic Jet Interaction on Missile Configurations. *Journal of Spacecraft and Rockets* **1998**, 35 (3), 296–302.
16. Graham, M. J.; Weinacht, P.; Brandeis, J. Numerical Investigation of Supersonic Jet Interaction for Finned Bodies. *Journal of Spacecraft and Rockets* **2002**, 39 (3), 376–383.
17. DeSpirito, J. Lateral Jet Interaction on a Finned Projectile in Supersonic Flow. *AIAA 50th Aerospace Sciences Meeting*, Nashville, TN, January 2012.
18. McMichael, J.; Lovas, A.; Plostins, P.; Sahu, J.; Brown, G.; Glezer, A. *Microadaptive Flow Control Applied to a Spinning Projectile*, AIAA-2004-2512.
19. Fresconi, F. E. Guidance and Control of a Projectile with Reduced Sensor and Actuator Requirements. *Journal of Guidance, Control, and Dynamics* **2001**, 34 (6), 1757–1766.
20. Cooper, G. R.; Fresconi, F. E.; Costello, M. F. Flight Stability of an Asymmetric Projectile with Activating Canards. *Journal of Spacecraft and Rockets* **2012**, 49 (1), 130–135.
21. Fresconi, F. E.; Harkins, T. Experimental Flight Characterization of Asymmetric and Maneuvering Projectiles from Elevated Gun Firings. *Journal of Spacecraft and Rockets* **2012**, 49 (6), 1120–1130.
22. Fresconi, F. E.; Celmins, I.; Ilg, M.; Maley, J. Roll Dynamics and Control with a Low Cost Skid-to-Turn Maneuver System. *Journal of Spacecraft and Rockets* **2014**.
23. Brown, T. G.; Davis, B.; Hepner, D.; Faust, J.; Myers, C.; Muller, P.; Harkins, T.; Hollis, M.; Miller, C.; Placzankis, B. Strap-Down Microelectromechanical (MEMS) Sensors for High-G Munition Applications. *IEEE Transactions on Magnetics* **2001**, 37 (1), 336–342.
24. Carlucci, D. E.; Frydman, A. M.; Cordes., J. A. Mathematical Description of Projectile Shot Exit Dynamics (Set Forward). *Journal of Applied Mechanics* **2013**, 80, 031501-1-9.
25. Celmins, I. *Design and Evaluation of an Electromechanical Actuator for Projectile Guidance*; ARL-MR-672; U.S. Army Research Laboratory: Aberdeen Proving Ground, MD, 2007.
26. Massey, K. C.; Siltan, S. I. Combining Experimental Data, Computational Fluid Dynamics, and Six-Degree of Freedom Simulation to Develop a Guidance Actuator for a Supersonic Projectile. *Journal of Aerospace Engineering* **2009**, 223, 341–355.
27. Fresconi, F.; Celmins, I.; Nelson, B. *Preliminary Characterization of Man Portable Precision Maneuver Concepts*; U.S. Army Research Laboratory Technical Report in progress, Aberdeen Proving Ground, MD, 2013.

28. Fairfax, L.; Fresconi, F.; Celmins, I.; Hathaway, W.; Steinhoff, M. Man Portable Precision Launch and Flight Trade Analysis, unpublished study, 2012.
29. Arrow Tech Associates. *PRODAS User Manual*, South Burlington, VT, 1997.
30. Guidos, B. G.; Celmins, I. *The 40-mm M433 Projectile Aerodynamics Obtained from Spark Range Firings*; ARL-TR-4619; U.S. Army Research Laboratory: Aberdeen Proving Ground, MD, 2008.
31. DeSpirito, J. U.S. Army Research Laboratory technical report in preparation.
32. Metacomp Technologies, Inc. *CFD<sup>++</sup> User Manual*, Agoura Hills, CA, 2012.
33. Menter, F. R. Two-Equation Eddy-Viscosity Turbulence Models For Engineering Applications. *AIAA Journal* **August 1994**, 32 (8), 1598–1605.
34. Chien, K.-Y. Predictions of Channel and Boundary Layer Flows with a Low-Reynolds-Number Turbulence Model. *AIAA Journal* **January 1982**, 20 (1), 33–38.
35. Metacomp Technologies, Inc. *MIME User Manual*, Agoura Hills, CA, 2011.
36. Weinacht, P.; Sturek, W. B.; Schiff, L. B. Navier-Stokes Predictions of Pitch Damping for Axisymmetric Projectiles. *AIAA Journal of Spacecraft and Rockets* November–December 1997, 34 (6), 753–761.
37. DeSpirito, J.; Sifton, S.; Weinacht, P. Navier-Stokes Predictions of Dynamic Stability Derivatives: Evaluation of Steady-State Methods. *Journal of Spacecraft and Rockets* **2009**, 46 (6), 1142–1154.
38. Bhagwandin, V. A; Sahu, J. Numerical Prediction of Pitch Damping Derivatives for a Finned Projectile at Angles of Attack. *AIAA Aerospace Sciences Meeting*, AIAA 2012-691, Nashville, TN, 2012.

---

## List of Symbols, Abbreviations, and Acronyms

---

AFRL	U.S. Air Force Research Laboratory
ARL	U.S. Army Research Laboratory
CFD	computational fluid dynamics
CP	center-of-pressure
DOD	Department of Defense
DOF	degree(s) of freedom
DSRC	DOD Supercomputing Resource Center
ERDC	U.S. Army Engineering Research and Development Center
HLLC	Harten-Lax-Van Leer-Contact
ISA	International Standard Atmosphere
L/D	length-to-diameter
NACA	National Advisory Committee for Aeronautics
PRODAS	Projectile, Rockets, and Ordnance Design and Analysis System
RANS	Reynolds-Averaged Navier-Stokes
SEAP	semiempirical aeroprediction
SST	Shear Stress Transport
TVD	Total-Variation-Diminishing
WT	wind tunnel

NO. OF  
COPIES ORGANIZATION

1 DEFENSE TECHNICAL  
(PDF) INFORMATION CTR  
DTIC OCA

1 DIRECTOR  
(PDF) US ARMY RESEARCH LAB  
IMAL HRA

1 DIRECTOR  
(PDF) US ARMY RESEARCH LAB  
RDRL CIO LL

1 GOVT PRINTG OFC  
(PDF) A MALHOTRA

1 RDRL WML E  
(PDF) F FRESCONI

INTENTIONALLY LEFT BLANK.